Chapter 3

Thermal Ignition and Flame Propagation from a Concentrated Hot Surface

3.1 Introduction

Hot surface ignition includes ignition by hot wires, pipes carrying hot gases, or malfunctioning equipment generating heat. One area of particular concern is the aviation industry where flammable mixtures can ignited by sufficiently hot surface in the fuel tank or surrounding flammable leakage zones. For aviation applications ignition may occur at any altitude, and therefore a range of pressures and fuel-air mixtures should be investigated.

Ignition of a gaseous mixture from a rapidly-heated hot surface of small spatial extent occurs in an inhomogeneous atmosphere in contrast to the homogeneous situation examined in Chapter 2. There are very significant gradients of temperature next to the ignition surface that play an essential role in the ignition process. We showed in the previous chapter that homogeneously heated mixtures can be modeled as a zero-dimensional problem and reasonable results obtained for ignition behavior considering only species and energy balances for the entire volume. Ignition by a hot surface requires multidimensional calculations of the fluid mechanics, heat transfer, species transport, and chemical reactions. It is necessary to perform experiments that test specific conditions of interest in order to obtain reliable results for ignition limits of hydrocarbon fuels like Jet A. Experiments also provide valuable data for testing numerical simulations of ignition based on approximate reaction mechanisms.

The approach taken in this study is to control the composition and pressure of the mixture and power input to the hot surface in order to control the peak surface temperature and determine

ignition thresholds.

Key measured properties include the temperature of the hot surface leading to ignition, the subsequent flame propagation speed and shape, and finally the resulting peak pressure.

3.2 Experimental Setup

The experiment uses a closed 2 liter combustion vessel. For each experiment the vessel is evacuated and filled with hexane, oxygen, and nitrogen using the method of partial pressures to create a specified mixture (accurate to 0.01 kPa). The mixture is then mixed using a circulation pump for 2 minutes, and left to settle for 2 minutes before increasing the temperature of the hot surface. Several different hot surfaces are used in the study, but the majority of the ignition temperature data are obtained from a Bosch high-temperature glow plug (noncommerical) and an Autolite 1110 glow plug (commercially available).

The schematic in Figure 3.1 shows a cross section view of the combustion vessel used in the experiment. The inside of the vessel is a rectangular prism with inner dimensions of 11.4 cm $\times$ 11.4 cm $\times$ 17.1 cm (width $\times$ depth $\times$ height) giving an internal volume of approximately 2 liters. Four access ports, including two windows, as shown in Figure 3.2 allow for schlieren visualization and simultaneous access for temperature measurements.

The hot surface is mounted inside the field of view of the schlieren system with a reference-stagnation surface visible at the lower edge (see Figures 3.1 and 3.4). The diameter of the surface is 58 mm, slightly smaller than the window diameter. The mounting fixture is made of aluminum and the stagnation surface limits the gas motion and helps facilitate the comparison with simulations, which do not consider the volume beneath the stagnation surface.

During an experiment, the temperatures at glow plug as well as at the top of the vessel are measured with K-type thermocouples, with response times of 0.5 s and approximately 1 s, respectively. The pressure is measured with a fast-response ($\geq$ 10 kHz) pressure gage (Endevco Model 8530B-200) at the top of the vessel.

A schlieren technique is used to visualize the plume of hot gas generated from the hot surface and the flame front. Settles (2001) has a detailed description of many different schlieren techniques. We usually used a typical schlieren system with a vertical and horizontal knife edge or dark background schlieren system (see Figure 3.5). A schematic of the setup used is given in Figure 3.3. Figure 3.4 shows an example of a color schlieren image that is obtained by placing a four color slide at the focus of the schlieren mirror. In all cases, we exploit the fact that the sharp density gradient across the

flame front changes the index of refraction of the gas and deflects the collimated light beam passed through the test section, creating the schlieren effect.

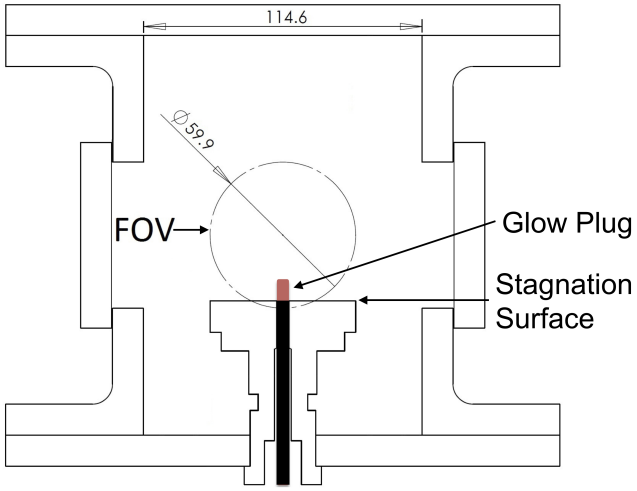

Figure 3.1: Diagram of the vessel, flow plug mounting fixture with stagnation surface, field of view (FOV), and glow plug (in red), with dimensions in mm

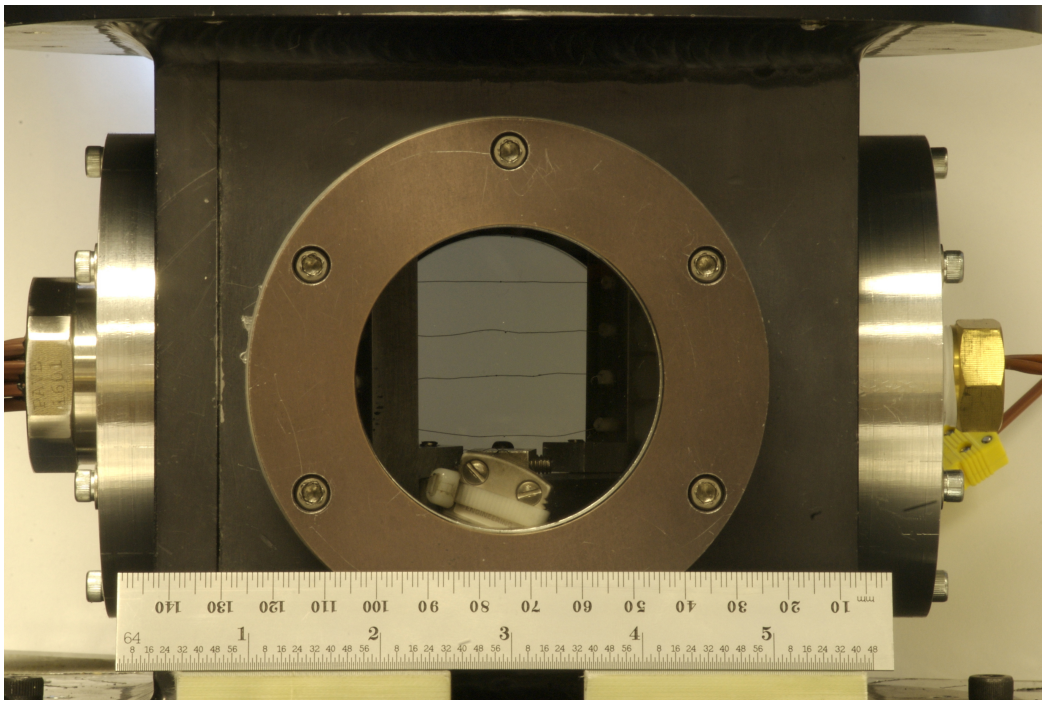

Figure 3.2: Photograph of the hot surface ignition vessel with an array of thermocouples above the hot surface. The flange on the left side shows a feedthrough for array of thermocouples and the feedthrough on the right is used for the thermocouple measuring the temperature of the hot surface.

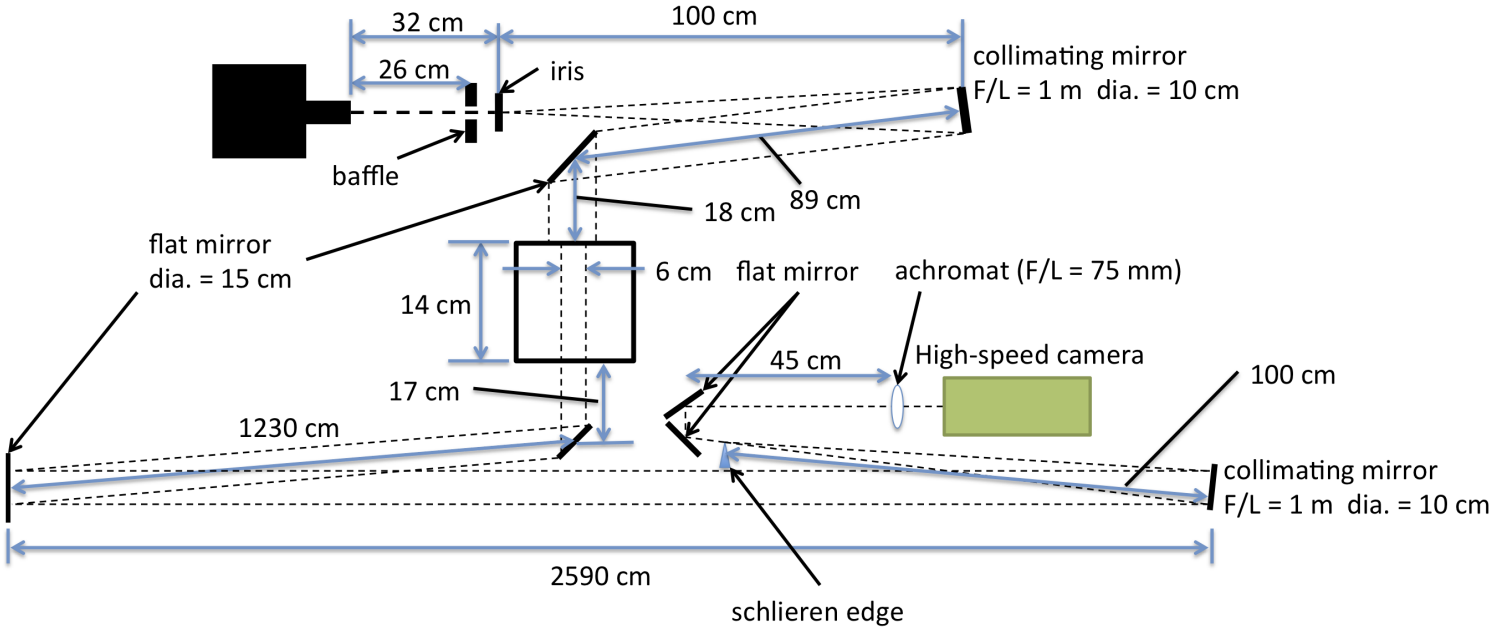

Figure 3.3: Schlieren setup schematic (the camera is used without a compound lens attached to the camera - the image is focused directly onto the CMOS with the 75 mm F/L lens)

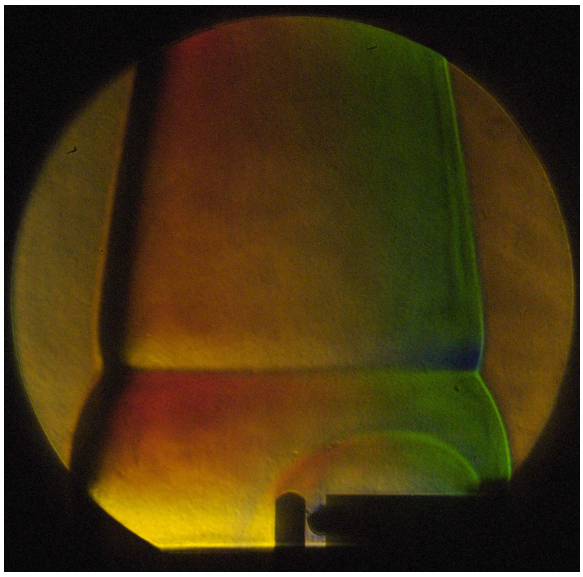

Figure 3.4: Example of color schlieren picture taken during the flame propagation of a hexane-air mixture at an equivalence ratio of $\phi = 1.9$, and initial pressure of $P_0 = 101$ kPa

Figure 3.5 shows a few frames from the high-speed schlieren video. From the video, we can confirm that the mixture ignited and at what time. The video is synchronized with the temperature and pressure measurements so that the ignition temperature can be identified. Additionally, the flame propagation speed is inferred from the video and the size of the window ($\varnothing$ = 59.9 mm/2.36 in) is used as the reference scale.

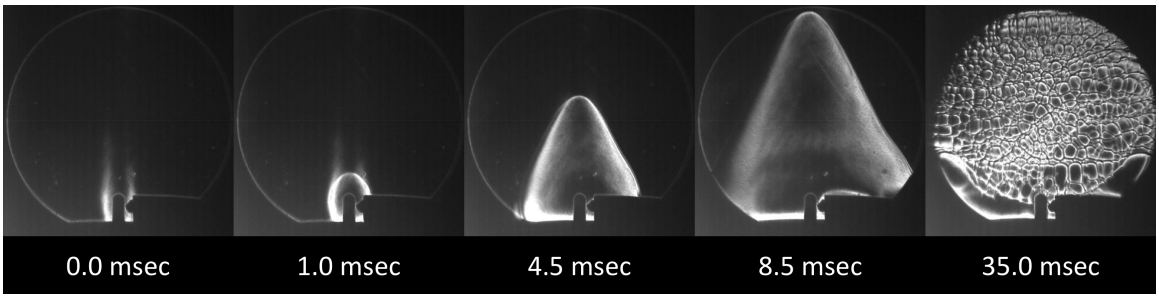

Figure 3.5: Dark background schlieren visualization of the flame propagation of shot 24 for a hexane-air mixture ($\phi = 1.2$). Typical frame rates were 1000–2000 frames per second (fps) using a 800 $\times$ 800 pixel resolution

The temperature measurement taken at the top of the vessel (Figure 3.6) gives an indication of the gas temperature before and after ignition. This measurement is mostly used for the initial temperature of the gas and to confirm whether or not ignition occurred in case other measurements should fail.

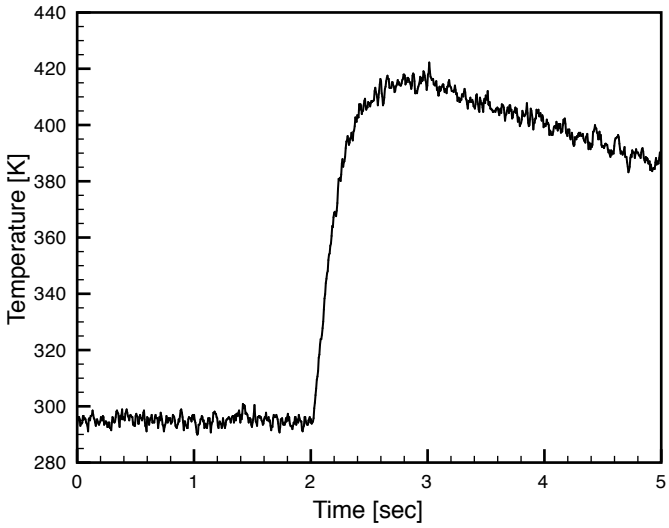

Figure 3.6: Temperature measurement at the top of the combustion vessel during the ignition of a hexane-air mixture ($\phi = 1.2$) initially at atmospheric pressure

The choice of hexane as the fuel for the experiments was motivated by its strong similarities to aviation and industrial hydrocarbon fuels while remaining simpler to handle experimentally. The hexane sample used in the experiments was characterized by the manufacturer as 89% n-hexane and 11% other hexane isomers. Mixtures of n-hexane/air are of interest at atmospheric pressure and lower, with equivalence ratios varying from the lower flammability limit at $\phi = 0.56$ to $\phi = 3.0$, corresponding to fuel concentrations from 1.2 to 6.48% (Zabetakis, 1965). At atmospheric and room temperature, the maximum partial pressure of hexane used was 6.5 kPa, which is well below the hexane room temperature vapor pressure of 15.6 kPa (Reid et al., 1977), and thus none of the fuel is expected to condense.

3.2.1 Composition Uncertainties

As described in the experimental procedure, the composition of the fuel-air mixture is controlled by filling the initially evacuated vessel using the method of partial pressures. The main uncertainty in the composition can be attributed to the accuracy of the pressure readings of 0.1 Torr (0.01 kPa). As part of the experimental procedure, deviations from the targeted pressure of 0.2 Torr were deemed acceptable. Some uncertainty in the composition is also created by the possibility of dissolving oxygen in the fuel.

However, additional uncertainty is created by the experimental setup, whose schematic is depicted in Figure 3.7. In the mixture preparation process, n-hexane is injected first to vaporize the liquid fuel,

and then oxygen and nitrogen are added in turn to create a fuel-air mixture. When the circulation pump is turned on next, the space between valve V3 and the tee to its right in the plumbing system (highlighted in Figure 3.7) will not be fully mixed with the rest of the system. While the exact mixture trapped in this dead space is not known, it reasonable to assume that the fuel will be compressed into this volume until the amount of oxygen is sufficient to reach the junction to the right of V3. This leads to a reduction in the amount of hexane injected by 1.7 % from the values reported in Appendix I.2. In this chapter, the composition has been adjusted to account for the shift in equivalence ratio just described. The maximum uncertainty is even greater ($\sim 10\%$) considering that more of the fuel could be pushed into the dead space mentioned. Combining this uncertainty with the others gives an overall uncertainty of +3%/-13% in terms of ϕ, which is either given as part of the error bars on the equivalence ratio or mentioned in the caption below each figure.

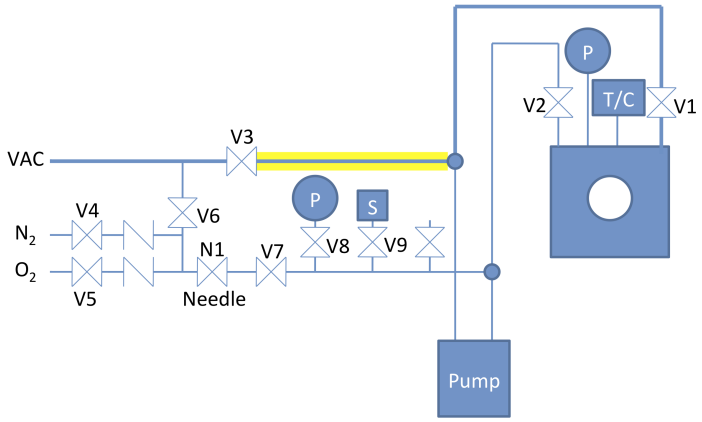

Figure 3.7: Hot surface experiment plumbing diagram (V–ball valve, VAC–vacuum pump, P–pressure transducer, T/C–thermocouple, S–Septum, Needle–needle valve for metering input)

3.2.2 Peak Pressure

The pressure during combustion is recorded with a fast-response pressure transducer at the top of the vessel. Pressure measurements such as the one shown in Figure 3.8 are important in assessing the potential structural damage that could be caused by an explosion. These measurements can be compared to constant-volume adiabatic equilibrium calculation performed with Cantera (Goodwin, 2003) as shown in Figure 3.9. Heat transfer during the combustion results in the experimental pressure being lower than those predicted by a constant-volume equilibrium calculation (Shepherd and Ratzel, 1985). At higher equivalence ratios, $\phi > \sim 2$, the flame speed is reduced, increasing the time for losses to occur and increasing the effect of buoyancy thus consuming a decreasing fraction

the mixture and reducing the peak pressure significantly below that predicted by the equilibrium calculation.

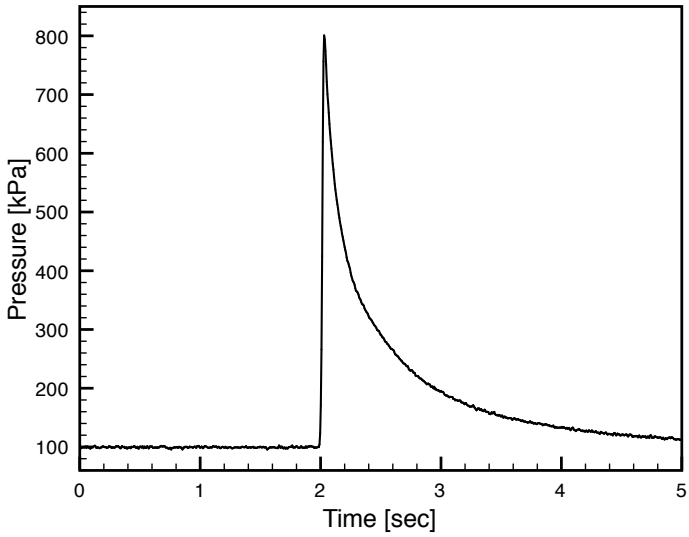

Figure 3.8: Pressure during the ignition of a hexane-air mixture ($\phi = 1.2$) initially at atmospheric pressure. The pressure is measured at the top of the combustion vessel. The peak pressure measured is 802.2 kPa.

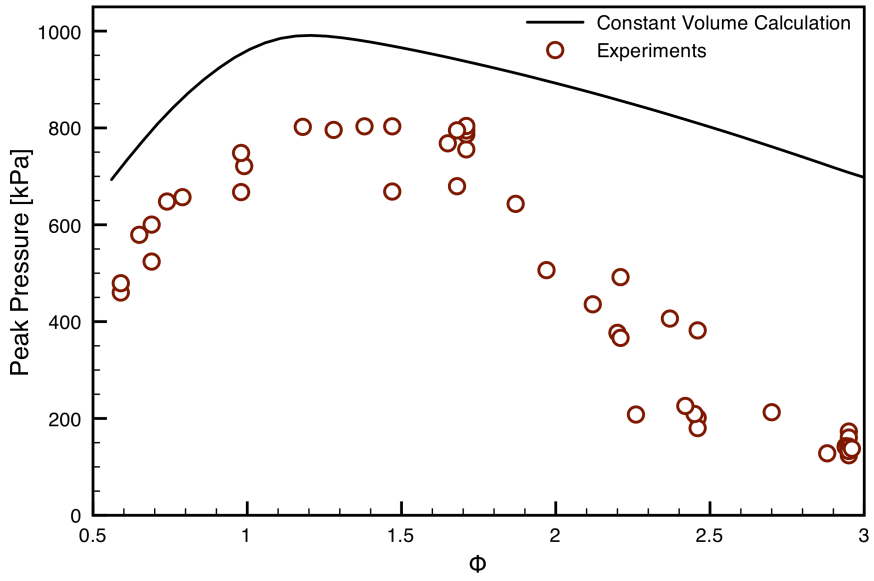

Figure 3.9: Peak pressure as a function of equivalence ratios at $P_0 = 101$ kPa. Experimental results and equilibrium calculations performed using Cantera (Goodwin, 2003). All mixture compositions have the associated uncertainty in ϕ of +3%/-13%, not shown here.

3.2.3 Hot Surface I — High-Temperature Glow Plug (Bosch)

One of the hot surfaces used in this study is a specialized high-temperature glow plug (Bosch Part number: 978801-0485). The geometry of the glow plug is shown in Figure 3.10, and typical temperature traces as a function of time are shown in Figure 3.11. This glow plug reaches temperatures in excess of 1000 K in 10 seconds and temperatures of above 1500 K after 30 seconds. During typical operation the glow plug was not powered for more than 30 seconds to prolong its lifetime. This glow plug was used for a large number of experiments. After these experiments, temperature measurements along the glow plug were taken to characterize its temperature distribution and during this the glow plug failed. Unfortunately only one such glow plug was available. Most of the remaining experiments were performed with a commercially available glow plug.

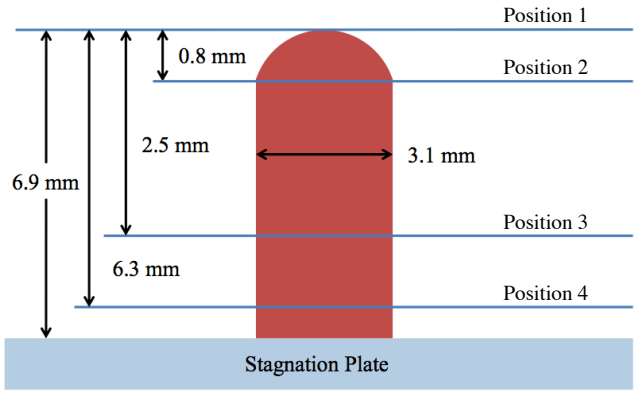

Figure 3.10: High-temperature glow plug schematic

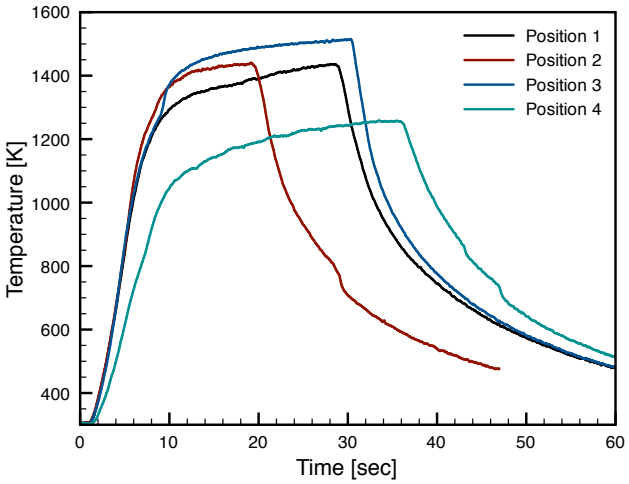

Figure 3.11: High-temperature glow plug temperature distribution

3.2.4 Hot Surface II — Standard Glow Plug (Autolite 1110)

The other standard hot surface that was used in this test series is a commerial automobile (diesel) glow plug (Autolite 1110). It is placed inside the stagnation plate in a similar fashion to the high-temperature glow plug. The geometry is shown in Figure 3.12 and the temperature profile is shown in Figure 3.13. It can reach a maximum temperature of 1453 K which fixed the upper limit of ignition temperature we were able to test.

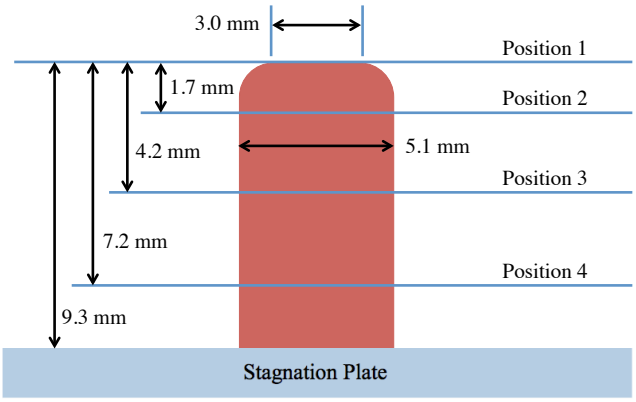

Figure 3.12: Autolite glow plug schematic

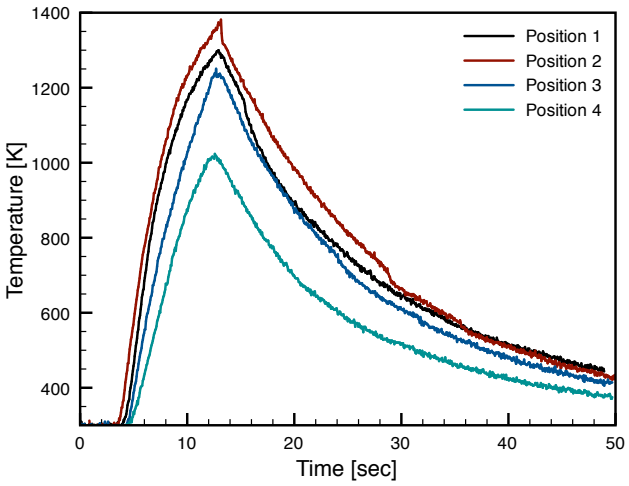

Figure 3.13: Autolite glow plug temperature distribution

3.3 Ignition Temperature

In this section, we investigate how the ignition temperature changes as a function of the fuel-air mixture, the initial pressure, and surface area of the hot surface. The hot surface temperature monitored during the experiment at the hottest part of the glow plug by a K-type thermocouple (bead size: $\varnothing = 0.3$ mm). The glow plug has an approximately 5 second temperature ramp before ignition. Figure 3.14 shows example of the measured glow plug temperature, beginning at the latter half of the temperature ramp. The ignition temperature of the gas mixture is defined as the temperature of the glow plug at the time ignition occurs. Ignition occurs at around 2 seconds as seen in the sharp increase in temperature slope. The exact time of ignition is inferred from the accompanying schlieren video. This confirms that the ignition coincides with the change in slope seen in the temperature reading. However, because the thermocouple has a response time of 0.5 seconds and the temperature of the glow plug is ramped up at ≈ 220 K/s, the ignition temperature has an uncertainty of +110 K from the measured value.

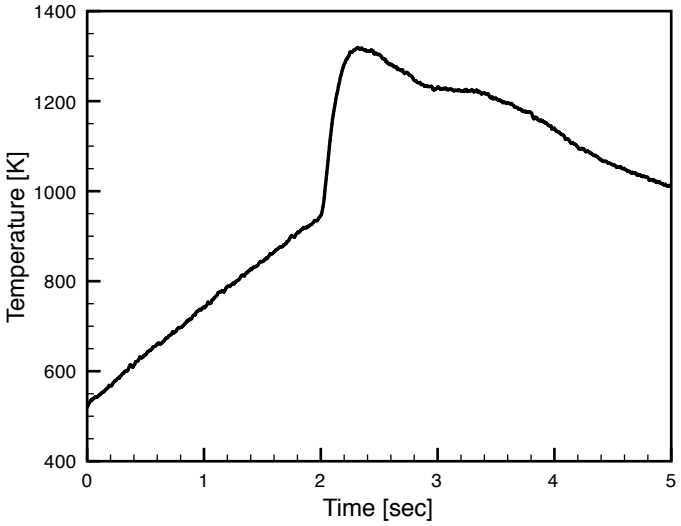

Figure 3.14: Temperature of the glow plug during the ignition of a hexane-air mixture ($\phi = 1.2$) initially at atmospheric pressure

Experiments with and without a thermocouple on the glow plug were performed to check if the presence of the thermocouple has an effect on the glow plug performance. Schlieren images show that the ignition location, which occurs on the top of the glow plug or its side, is not affected by the presence of the thermocouple (see Appendix J). From these images we conclude that the effect of the thermocouple is negligible as the substantial variability in ignition location is unbiased.

3.3.1 Hot Surface Ignition Temperature as a Function of Composition

A systematic study has been performed using the Bosch glow plug investigating the ignition temperature as a function of composition expressed by the equivalence ratio, ϕ, at atmospheric pressure. Additional experiments have been performed using the Autolite glow plug and a small strip of electrically heated nickel foil. The minimum ignition temperature is observed to be essentially constant at 920 K $\pm$ 20 K for equivalence ratios in the range of $\phi = 0.75 - -3.0$ as shown in Figure 3.15. Large increase and variability in the ignition temperature is observed at the extreme lean ($\phi \sim 0.6$) and rich ($\phi \sim 3.0$) conditions. Consistent with the literature (Zabetakis, 1965), the lower flammability limit is observed to be less than $\phi = 0.6$ with a mixture at $\phi = 0.5$ not igniting after heating for 30 seconds and the glow plug reaching 1520 K. In the literature the upper flammability limit of n-hexane in air is given as 7.4 %, $\phi = 3.4$ (Zabetakis, 1965). We saw significant variability in ignition temperature at $\phi = 3.0$, but did not explore richer mixtures to confirm the flammability limit. The source of the variability in ignition temperature near $\phi = 3.0$ when using the Autolite glow plug is not clearly understood and should be considered for future study.

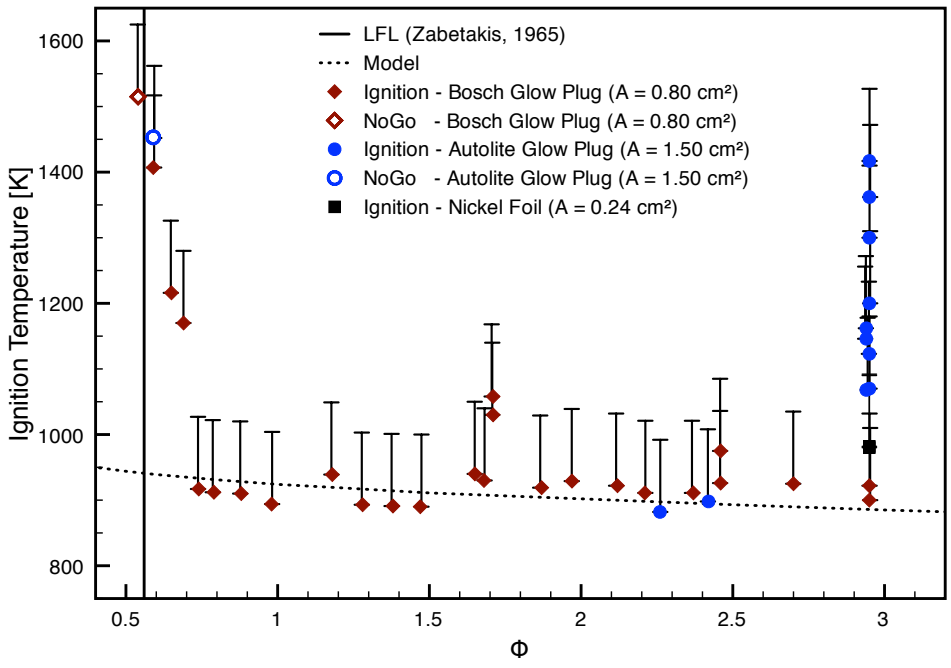

Figure 3.15: Hot surface ignition temperature as a function of equivalence ratio at atmospheric pressure for different hot surface sizes. The uncertainty associated with the ignition temperature stems from the ramp rate of the glow plug of $\approx$ 220 K/sec and the response time of the thermocouple of 0.5 seconds. All mixture compositions have the associated uncertainty of +3%/-13% in ϕ, not shown here.

In addition to the experiments, we present in Figure 3.15 the results of a simple model for ignition (discussed in the next section). The model captures the minimum ignition temperature and shows a weak dependence on composition, but does not describe the lower or upper flammability limit.

3.4 Ignition Modeling

3.4.1 Modeling Background

Modeling and predicting the ignition process near a hot surface requires considering the spatial and temporal evolution of the species and temperature of the gas. Simplified approaches are possible, but for an accurate prediction it is necessary to solve the fluid mechanical and chemical equations simultaneously on a grid sufficiently small to resolve the thermal and fluid dynamical boundary layer around the hot surface as well as including the low-temperature chemistry that has a critical influence on the ignition process as detailed in Chapter 2. An additional feature of nonhomogeneous ignition is the differential diffusion of species, a large range of molecular weights exists in the gas mixtures, which is challenging to accurately simulate.

The main approaches to modeling hot surface ignition have been to use one-dimensional conduction equation with heat-release from the chemical reactions. Extensions of this are 2-dimensional steady simulations as done by Adler (1999) and unsteady simulations like the ones performed by Kumar (1989).

Adler (1999) modeled the problem of a circular hot spot, e.g., from a laser, in contact with a combustible mixture. In his model one, of the main assumptions is that the heated layer of gas is stagnant and thus the problem is governed by the energy equation including heat conduction and energy release from the chemical reactions, which in its steady form is usually referred to as the Frank-Kamenetskii problem (Glassman, 2008).

3.4.2 Simplified Analytical Approach

The minimum ignition temperature may be estimated using a simple analytical model such as that proposed by Laurendeau (1982). An additional discussion of hot surface ignition as developed by Semenov (1940) and Kuchta et al. (1965) are given in Appendix E.

The Laurendeau model proposes that ignition occurs when the rate of heat-loss from the reacting mixture just balance the energy release by chemical reactions. The steady one-dimensional energy

conservation equation with chemical energy release is modeled as

$$Qr_f = -k\frac{d^2T}{dx^2} \ , \tag{3.1}$$

where k is the thermal conductivity coefficient, Q is the chemical energy release, and r_f is the reaction rate given by an empirical model that is slightly more sophisticated than the ones presented in the previous chapter and includes a dependency on composition and density, but without reactant consumption

$$r_f = -X_F^{m_f} X_O^{m_o} \rho^n A \exp\left[-\frac{E_a}{\tilde{R}T}\right] \ . \tag{3.2}$$

X_F and X_O are the initial mole fraction of the fuel and oxidizer, respectively; ρ is the density and $n = m_f + m_o$ is the reaction order. Equation 3.1 is integrated across a stagnant thermal boundary layer subject to the following boundary conditions:

$$x = 0, \ \ T = T_w, \tag{3.3}$$

$$x = \delta, \ \ T = T_e, \tag{3.4}$$

where the wall at $x = 0$ is at the wall temperature, T_w, and outside the boundary layer ($x = \delta$), the temperature is relaxes back to the ambient temperature, T_e. Laurendeau (1982) evaluates the density at a geometric mean temperature given by

$$\rho = \frac{P}{\tilde{R}\sqrt{T_w T_e}} \tag{3.5}$$

Prior to integrating Equation 3.1, it is multiplied by $(dT/dx)dx = dT$

$$k\frac{d^2T}{dx^2}\frac{dT}{dx}dx = QX_F^{m_f} X_O^{m_o} \rho^n A \exp\left[-\frac{E_a}{\tilde{R}T}\right] dT \tag{3.6}$$

making the integration of the left-hand side into a spatial integral and the right-hand side into a temperature integral.

$$k\int_0^\delta \left(\frac{d^2T}{dx^2}\right)\left(\frac{dT}{dx}\right) dx = AQX_F^{m_f} X_O^{m_o} \rho_e^n \left(\frac{T_e}{T_w}\right)^{n/2} \int_{T_w}^{T_e} \exp\left[-\frac{E_a}{\tilde{R}T}\right] dT \tag{3.7}$$

Using the chain rule, the left-hand side can be simplified and integrated.

$$k\int_0^\delta \left(\frac{d^2T}{dx^2}\right)\left(\frac{dT}{dx}\right)dx = k\int_0^\delta \frac{1}{2}\frac{d}{dx}\left(\frac{dT}{dx}\right)^2 dx = \frac{k}{2}\left[\left(\frac{dT}{dx}\right)^2\right]_0^\delta \tag{3.8}$$

The spatial derivative of the temperature is zero as we leave the boundary layer, i.e., at $x = \delta$. Absorbing the minus sign into the integration order of the right-hand side the energy equation becomes

$$k\left(\frac{dT}{dx}\right)_w^2 = 2AQX_F^{m_f}X_O^{m_o}\rho_e^n\left(\frac{T_e}{T_w}\right)^{n/2}\int_{T_e}^{T_w}\exp\left[-\frac{E_a}{\tilde{R}T}\right]dT\ . \tag{3.9}$$

In order to evaluate the integral, the standard large activation energy approximation as discussed in previous chapter and Appendix C.2.2 can be made:

$$T = T_w + T',\ \ (T' < 0) \tag{3.10}$$

$$\exp\left[-\frac{E_a}{\tilde{R}T}\right] \cong \exp\left[-\frac{E_a}{\tilde{R}T_w} + \frac{E_a}{\tilde{R}{T_w}^2}T'\right] \tag{3.11}$$

Using this approximation, the energy equation simplifies to

$$k\left(\frac{dT}{dx}\right)_w^2 = 2AQX_F^{m_f}X_O^{m_o}\rho_e^n\left(\frac{T_e}{T_w}\right)^{n/2}\exp\left[-\frac{E_a}{\tilde{R}T_w}\right]\int_{T_e-T_w}^0\exp\left[\frac{E_a}{\tilde{R}{T_w}^2}T'\right]dT'\ , \tag{3.12}$$

where by noting that $(T_e - T_w)$ is negative, the integral becomes

$$\int_{-(T_w-T_e)}^0\exp\left[\frac{E_a}{\tilde{R}{T_w}^2}T'\right]dT' = \left(\frac{\tilde{R}{T_w}^2}{E_a}\right)\left(1-\exp\left[-\frac{E_a}{\tilde{R}{T_w}^2}\left(T_w-T_e\right)\right]\right) \approx \left(\frac{\tilde{R}{T_w}^2}{E_a}\right)\ . \tag{3.13}$$

Recall that the upper integration limit refers to the wall temperature (see Equation 3.9), which dominates the energy release due to the high-activation energy assumption. Finally, the energy equation is

$$k\left(\frac{dT}{dx}\right)_w^2 \approx 2AQX_F^{m_f}X_O^{m_o}\rho_e^n\left(\frac{T_e}{T_w}\right)^{n/2}\exp\left[-\frac{E_a}{\tilde{R}T_w}\right]\left(\frac{\tilde{R}{T_w}^2}{E_a}\right)\ , \tag{3.14}$$

so that for steady-state conditions, the heat flux from the gas to the wall due to chemistry is

$$q_{\text{chem}} = k\left(\frac{dT}{dx}\right)_w = \sqrt{2kAQX_F^{m_f}X_O^{m_o}\rho_e^n\left(\frac{T_e}{T_w}\right)^{n/2}\exp\left[-\frac{E_a}{\tilde{R}T_w}\right]\left(\frac{\tilde{R}{T_w}^2}{E_a}\right)}\ . \tag{3.15}$$

Laurendeau proposes that this must be equal to the heat flux from the wall to the gas as modeled

by an engineering correlation

$$q_{\text{loss}} = \frac{kNu}{L}\left(T_{\text{wall}} - T_e\right) \ . \tag{3.16}$$

The condition for ignition is given as (Laurendeau, 1982)

$$q_{\text{chem}} = q_{\text{loss}} \ . \tag{3.17}$$

Depending on the flow condition (stagnant, free or forced convection) the expression for the Nusselt number, Nu, changes. For example, for stagnant mixtures, the Nusselt number is constant and thus the wall temperature scales inversely with the natural log of the length scale (Laurendeau, 1982, Semenov, 1940).

$$\ln L \propto \frac{E_a}{2\tilde{R}T_{\text{wall}}} \tag{3.18}$$

This dependence on surface size and the obvious limitations will be discussed further in subsequent sections (see Figure 3.26).

Law and Law (1979) discuss the problem of ignition in a steady boundary layer flow for mixtures with large activation energies. Their analysis shows that a locally similar region of balanced reaction and diffusion is present next to the wall, and a nonsimilar diffusion and convection balance outside this region. The problem is solved using the method of matched asymptotics, and the ignition behavior is presented as a function of the Damköhler number, the ratio of the fluid time scale to the chemical reaction time scale. The Damköhler number defined is the ratio of the heat-loss and chemical release described in Laurendeau (1982). Ignition is predicted to occur as the Damköhler number reaches unity.

3.4.3 Boundary Layer Modeling Approach [1]

The temperature at which the mixture ignites corresponds to a balance between heat-release due to chemical reactions and heat-loss due to diffusion and convection. An estimate of the ignition temperature may be determined by comparing the time scales of these processes. As the glow plug heats up the surrounding mixture, natural convection begins and a boundary layer develops on the surface of the glow plug. A fluid element passing through the boundary layer is heated up initiating chemical reaction, whose energy release is in competition with heat conduction and convection away

[1] A preliminary version of this work was presented at the Eighth International Symposium on Hazards, Prevention, and Mitigation of Industrial Explosions (8^{th} ISHPMIE) in Yokohama, Japan: "Hot Surface Ignition of Hydrocarbons in Air — A Comparison of Experimental and Computational Results" (Philipp A. Boettcher, Brian Ventura , Guillaume Blanquart, and Joseph E. Shepherd).

from the fluid element.

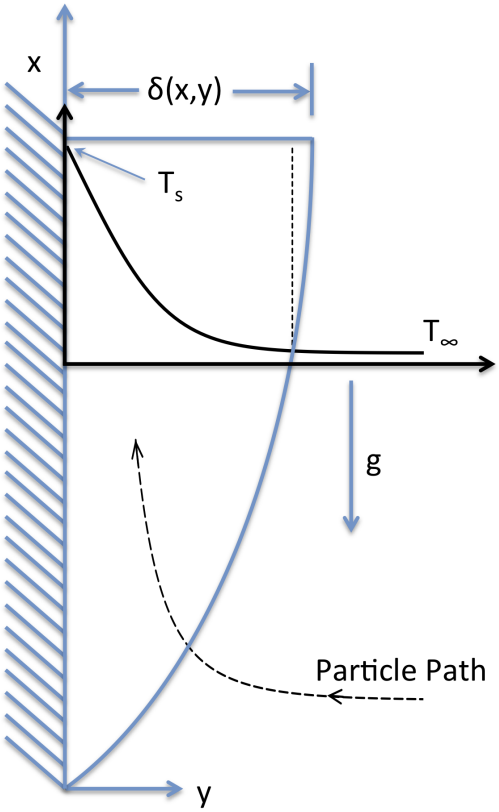

Figure 3.16: Thermal boundary layer along a vertical hot plate

The full governing equations are adapted from Kee et al. (2003) for Cartesian coordinates.

Continuity:

$$\frac{\partial \rho}{\partial t} + \frac{\partial}{\partial x}(\rho u) + \frac{\partial}{\partial y}(\rho v) = 0 \tag{3.19}$$

x - Momentum:

$$\rho \frac{\partial u}{\partial t} + \rho u \frac{\partial u}{\partial x} + \rho v \frac{\partial u}{\partial y} = -\frac{\partial P}{\partial x} + \mu \left(\frac{\partial^2 u}{\partial x^2} + \frac{\partial^2 u}{\partial y^2} \right) + \rho g \beta (T - T_\infty) \tag{3.20}$$

y - Momentum:

$$\rho \frac{\partial v}{\partial t} + \rho u \frac{\partial v}{\partial x} + \rho v \frac{\partial v}{\partial y} = -\frac{\partial P}{\partial y} + \mu \left(\frac{\partial^2 v}{\partial x^2} + \frac{\partial^2 v}{\partial y^2} \right) \tag{3.21}$$

Energy:

$$\rho c_p \frac{\partial T}{\partial t} + \rho u c_p \frac{\partial T}{\partial x} + \rho v c_p \frac{\partial T}{\partial y} = u \frac{\partial P}{\partial x} + \frac{\partial}{\partial y}\left(k \frac{\partial T}{\partial y}\right) - \sum_{k=1}^{K_g} \rho c_{pk} Y_k V_{k_y} \frac{\partial T}{\partial y} - \sum_{k=1}^{K_g} \dot{\omega}_k W_k h_k \tag{3.22}$$

In general, these equation have to solved by numerical methods. To make analytical progress, a number of simplifying assumptions will be made. We will assume that density gradients are only important when multiplied by gravity (Boussinesq approximation). The volumetric expansion coefficient, β, will be evaluated at an average temperature value. We assume the gas is composed of only one species, which does not undergo any chemical composition change following Kaviany (2002). Additionally, we assume the boundary layer is laminar and steady and neglect pressure gradients along the x-axis. The boundary layer is also assumed to be thin, such that gradients in the y-direction are much greater than those in the x-direction, and that $u \gg v$. To estimate the time scales for energy release and energy loss, we consider the development of the boundary layer separately from the chemical energy release. This assumption simplifies our analysis and is somewhat justified by the Arrhenius rate dependence of the reaction rate on temperature, which implies that most of the chemical reaction occurs at elevated temperatures close to ignition. The resulting equations for a steady, non-reacting thermal boundary layer driven by buoyancy are:

Continuity:

$$\frac{\partial u}{\partial x} + \frac{\partial v}{\partial y} = 0 \tag{3.23}$$

x-Momentum:

$$\rho\left(u \frac{\partial u}{\partial x} + v \frac{\partial u}{\partial y}\right) = \rho g \beta \left(T - T_\infty\right) + \mu \frac{\partial^2 u}{\partial y^2} \tag{3.24}$$

y-Momentum:

$$\frac{\partial p}{\partial y} = 0 \tag{3.25}$$

Energy:

$$\rho c_p \left(u \frac{\partial T}{\partial x} + v \frac{\partial T}{\partial y}\right) = k \frac{\partial^2 T}{\partial y^2} \tag{3.26}$$

The boundary conditions are:

$$u(x,0) = v(x,0) = u(x,\infty) = 0 \tag{3.27}$$

$$T(x,0) = T_s \text{ and } T(x,\infty) = T_\infty \tag{3.28}$$

The most significant approximation, other than neglecting chemical reactions, is the assumption of constant density. This assumption introduces some error, but greatly simplifies the calculations, while still clearly illustrating the concept. Cairnie and Harrison (1982) present the variable density equations, which are more appropriate for large surface-to-ambient temperature differences. While the pressure remains constant the large temperature at the wall has a significant impact on the specific volume of the fluid close to the wall, which leads to a shift of the velocity and temperature away from the wall. This shift can be expressed by using Howarth-Dorodnitsyn (Stewartson, 1964) transformed coordinate

$$\bar{y} = \int_0^y \frac{\rho}{\rho_\infty} dy \ . \tag{3.29}$$

While this transformation is needed for accurate solutions, we do not consider this approach and only treat the ρ = constant case. Following the derivation given by Gebhart et al. (1988) a similarity solution for Equations 3.23-3.28 can be obtained by combining the spatial variable into a single nondimensional coordinate $\eta(x, y)$ described below

$$\eta = b(x)y \ , \tag{3.30}$$

where $b(x)$ is the function that links the scaling

$$b(x) = \frac{1}{x}\left[\frac{gx^3}{4\nu^2}\beta\left(T_s - T_\infty\right)\right]^{1/4} \ . \tag{3.31}$$

The velocities are expressed through a stream function, ψ

$$u = \psi_y \ \ v = -\psi_x \ \ \psi(x, y) = \nu c(x) f(x, y), \tag{3.32}$$

where $f(x, y)$ and $c(x)$ are nondimensional functions

$$c(x) = 4\left[\frac{gx^3}{4\nu^2}\beta\left(T_s - T_\infty\right)\right]^{1/4} \ . \tag{3.33}$$

The temperature is nondimensionalized via

$$T^* = \frac{T - T_\infty}{T_s - T_\infty} \ . \tag{3.34}$$

The functions $b(x)$ and $c(x)$ are found such that T^* and f are only functions of η while also satisfying

all of the boundary conditions (Gebhart et al., 1988).

The new non-dimensionalized momentum and energy equations are

$$f''' + 3ff'' - 2f'^2 + T^* = 0 \tag{3.35}$$

$$(T^*)'' + 3Prf(T^*)' = 0 \tag{3.36}$$

where $'$ denotes differentiation with respect to η. Pr is the Prandtl number

$$Pr = \frac{\nu}{\alpha} \, , \tag{3.37}$$

where α is the thermal diffusivity and ν is the kinematic viscosity. The stream function ψ is expressed as a function of the Grashof number based on x,

$$\psi(x,y) = 4\nu \left(\frac{Gr_x}{4}\right)^{1/4} f(x,y) \, , \tag{3.38}$$

$$Gr_x = \frac{g\beta(T_s - T_\infty)x^3}{\nu^2} \, , \tag{3.39}$$

and the similarity parameter η is

$$\eta = \frac{y}{x}\left(\frac{Gr_x}{4}\right)^{1/4} = \frac{y}{x^{1/4}}\left[\frac{g\beta(T_s - T_\infty)}{4\nu^2}\right]^{1/4} \tag{3.40}$$

The momentum and energy equations can be solved to give the velocity and temperature distribution as well as the boundary layer thickness along the plate. The temperature distribution is computed using the similarity solution as a function of the similarity parameter, η, as using the methods described in text books by Kaviany (2002) and Gebhart et al. (1988).

Figure 3.17 shows the temperature distribution away from the hot surface and indicates the edge of the laminar, viscous boundary layer at $\eta_{0.01} = 4.423$ defined as the point where $T^* = 0.01$. Equation 3.40 can be rearranged to solve for the boundary layer thickness, $y = \delta$, a given length, $x = L$, away from the start of the plate

$$\delta = \frac{\eta_\delta L}{(Gr_L/4)^{1/4}} \, . \tag{3.41}$$

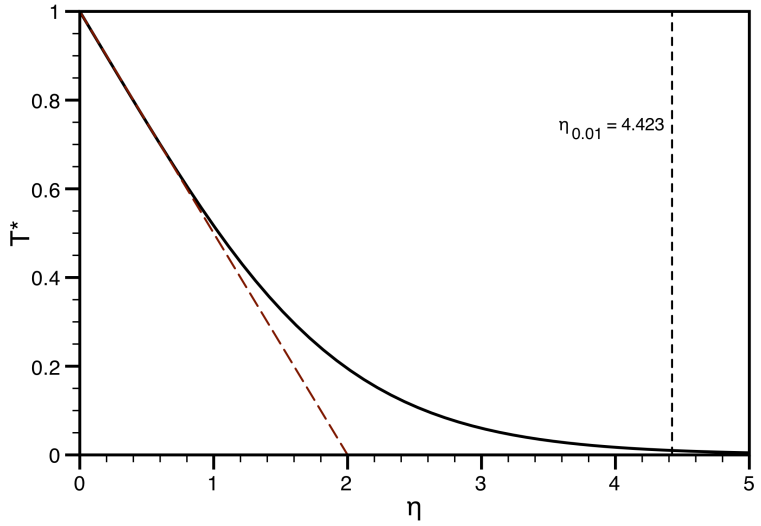

Figure 3.17: Temperature profile in a thermal boundary layer along a vertical hot plate (Pr = 0.72)

Using a simple dimensional analysis, we can extract an approximate time scale for heat conduction through the boundary layer. Squaring both sides of Equation 3.41 and multiplying by the Prandtl number allows for the following simplification.

$$\frac{\delta^2 \nu}{\alpha} = Pr \frac{\eta_\delta^2 L^2}{(Gr_L/4)^{1/2}} \tag{3.42}$$

$$\frac{\delta^2}{\alpha} = Pr \sqrt{\frac{4\eta_\delta^4 L^4}{Gr_L \nu^2}} \tag{3.43}$$

$$\frac{\delta^2}{\alpha} = Pr \sqrt{\frac{4\eta_\delta^4 L^4}{\nu^2} \frac{\nu^2}{g\beta(T_s - T_\infty)L^3}} \tag{3.44}$$

$$\frac{\delta^2}{\alpha} = Pr \sqrt{\frac{4\eta_\delta^4 L}{g\beta(T_s - T_\infty)}} \tag{3.45}$$

The characteristic time scale for heat conduction through the layer then becomes

$$\tau_{diff} = \frac{\delta^2}{\alpha} = Pr \sqrt{\frac{4\eta_\delta^4 L}{g\beta(T_s - T_\infty)}} \, . \tag{3.46}$$

Figure 3.17 shows that an approximation of the temperature profile as a linear function of η, which is consistent with defining $\eta_\delta = 2$, gives the diffusion time scale,

$$\tau_{diff} = 8\,Pr\sqrt{\frac{L}{\beta \Delta T g}} \tag{3.47}$$

where L is the height of the glow plug, β is the thermal expansion ratio, and ΔT is the temperature difference across the boundary layer ($T_s - T_\infty$). For a mixture with a Prandtl number of Pr = 0.72, we obtain $\tau_{diff} \approx 250$ ms.

The chemical time sale is found by computing the time to ignition of mixture of n-heptane and air at a given temperature assuming a constant pressure, adiabatic reactor. A mixture is initialized at a given temperature and the chemical heat-release is allowed to evolve, which leads to a temperature increase that can be captured by the energy equation

$$\frac{dT}{dt} = \frac{\dot{q}_r}{V \rho c_p} \tag{3.48}$$

and the ignition time, τ_{ign}, is defined as time elapsed until the maximum temperature increase rate is reached

$$t = \tau_{ign} \text{ when } \frac{dT}{dt} = \text{maximum} \,. \tag{3.49}$$

The computations were obtained using the detailed chemical mechanism of Curran et al. (1998) with the FlameMaster code (Pitsch and Bollig, 1994). Heptane was used in place of hexane since the chemistry of heptane is better understood, and previous studies have shown that normal alkanes share very similar ignition properties, such as the shock tube ignition delay time (Shen et al., 2009, Westbrook et al., 2009).

The ignition temperature is then defined as the initial temperature for which the ignition time, τ_{ign}, is equal to the diffusion time, τ_{diff}. For instance, as shown on Figure 3.18, a mixture with equivalence ratio $\phi = 1.0$ is predicted to ignite within 250 ms if the initial temperature is around 905 K. This analysis is repeated for several different equivalence ratios, and the predicted ignition temperatures are compared to the temperatures measured experimentally. As shown on Figure 3.15, both the experiments and the simple model predict a weak dependence of the ignition temperature on the equivalence ratio. This result is due to the weak dependence of ignition time on equivalence ratio. However, the model fails to predict the sudden rise in ignition temperature below $\phi = 0.7$. There could be multiple sources of discrepancies; for instance, the model accounts only for thermal diffusion and neglects diffusion of key combustion intermediates such as radicals.

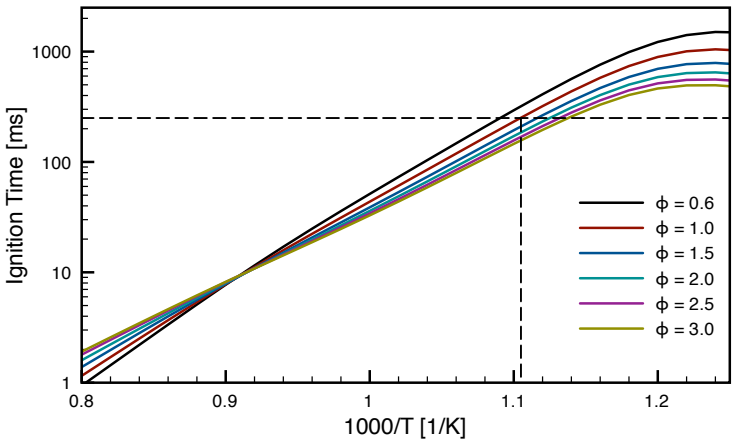

Figure 3.18: Ignition times for n-heptane and air mixtures at atmospheric pressure computed with the detailed chemical mechanism of Curran et al. (1998) ($\tau_{diff} = 250$ ms, $T = 905$ K indicated)

Temperature Profile Along Particle Trajectories While the scaling arguments just described give a simple model for estimating the ignition temperature, a more realistic model for the ignition event may be investigated by following an individual fluid element through the boundary layer. Using the similarity solution, we can obtain the trajectory of the fluid element. Recall the nondimensional equations for x-momentum, energy and the stream function, ψ, from Gebhart et al. (1988), which can be solved numerically.

$$f''' + 3ff'' - 2f'^2 + T^* = 0 \tag{3.50}$$

$$(T^*)'' + 3Prf(T^*)' = 0 \tag{3.51}$$

$$\psi(x,y) = 4\nu \left(\frac{Gr_x}{4}\right)^{1/4} f(x,y) \tag{3.52}$$

The viscosity and thermal conductivity are taken at the mean temperature, $(T_s + T_\infty)/2$ - 650 K in this example, using the data from Kadoya et al. (1985) and Stephan and Laesecke (1985), respectively.

Table 3.1: Parameters used in modeling of hexane-air hot surface ignition

Parameter		Units	Description
g	9.81	m s^{-2}	gravitational acceleration
T_s	1000	K	surface temperature
T_∞	300	K	gas temperature away from the wall
μ	3.257 $\times 10^{-5}$	Pa s	dynamic air viscosity at 650 K
ρ_0	0.57	kg m^{-3}	unburnt gas density at 650 K
ν	5.71 $\times 10^{-5}$	m^2 s	kinematic air viscosity at 650 K
β	1.54 $\times 10^{-3}$	K^{-1}	volumetric thermal expansion coefficient
k	4.862 $\times 10^{-2}$	W m^{-1} K^{-1}	thermal conductivity of air at 650 K
q_c	2.3×10^6	J kg^{-1}	stored chemical energy
c_p	1357	J kg^{-1} K^{-1}	average specific heat of the gas mixture at constant pressure
E_a	35075	cal kmol^{-1}	activation energy
	146754	J kmol^{-1}	activation energy
A	3.3×10^{14}	s^{-1}	pre-exponential

We can follow a given fluid element with an initial position (x_0, y_0) by computing the local velocity ($u(x,y)$, $v(x,y)$) and integrating the path.

$$x = x_0 + \int_0^t u(x,y)dt' \tag{3.53}$$

$$y = y_0 + \int_0^t v(x,y)dt' \tag{3.54}$$

From the definition of the stream function the velocities are computed

$$u = \frac{\partial \psi}{\partial y} = 4\nu \left(\frac{Gr_x}{4}\right)^{1/4} \frac{\partial f}{\partial \eta}\frac{\partial \eta}{\partial y} \tag{3.55}$$

$$v = -\frac{\partial \psi}{\partial x} = -\frac{4\nu}{4^{1/4}} \frac{\partial \left(Gr_x\right)^{1/4}}{\partial x} f - 4\nu \left(\frac{Gr_x}{4}\right)^{1/4} \frac{\partial f}{\partial \eta}\frac{\partial \eta}{\partial x} \tag{3.56}$$

where f, and $\partial f/\partial \eta$ are computed as part of the numerical solution. Away from the wall, in the outer layer, the temperature is low and the contribution of chemical energy release is negligible and the equations above correctly predict the temperature and flow path of a fluid element.

The chemical energy release becomes important at high-temperatures, which are found in a small inner layer next to the wall. If the chemical energy release is included in the energy equation, for

example, using a one-step model, the equation becomes

$$\rho c_p \left(u\frac{\partial T}{\partial x} + v\frac{\partial T}{\partial y} \right) - k\frac{\partial^2 T}{\partial y^2} = -q_c A \exp\left[-\frac{E_a}{\tilde{R}T} \right] . \tag{3.57}$$

The chemical energy release increases the fluid element temperature. This energy release is small until very high-temperatures due to the large activation energy, E_a. Before ignition occurs the energy release can be lost through either conduction or convection. At the wall, we can establish the dominant balance to find whether conduction or convection is responsible for the energy loss. A version of this calculation is given by Law and Law (1979). [2]

Near the wall both temperature and wall velocity are small, which can be expressed in the nondimensional parameters T^* and f.

$$T^* = T_w^* + \epsilon_1 \tilde{T}^* \tag{3.58}$$

$$f = f_w + \epsilon_2 \tilde{f} \tag{3.59}$$

Making the substitution above in the x-momentum equation, while noting that $f_w = 0$ due to the boundary conditions (nonporous wall and nonslip condition), gives

$$\epsilon_1 \tilde{f}''' + 3\epsilon_1^2 \tilde{f}\tilde{f}'' - 2\epsilon_1^2 \tilde{f}'^2 + T_w^* + \epsilon_1 \tilde{T}^* = 0 \tag{3.60}$$

which implies that the deviations are of the same magnitude $\epsilon_1 = \epsilon_2 = \epsilon$. Via the same substitution the energy becomes

$$\epsilon(\tilde{T}^*)'' + 3\epsilon^2 Pr \tilde{f}(\tilde{T}^*)' = -\tilde{q} \tag{3.61}$$

where $\tilde{q}$ is the nondimensional chemical energy release. From Equation 3.61 we can see that the dominant balance at the wall is between the chemical energy release rate and the thermal diffusion, with the convection an order of magnitude smaller.

Along the path we can now compute the heat transfer as well as the heat-release from a one-step model as well as the heat diffusion. As a simplifying assumption, we treat the heat-loss as the dominant in the y-direction so the heat transfer term of the energy equation is

$$k\frac{\partial^2 T}{\partial y^2} = k(T_s - T_\infty)\frac{\partial^2 T^*}{\partial \eta^2}\left(\frac{\eta}{y} \right)^2 . \tag{3.62}$$

[2] The author would like to thank Jason S. Damazo for his significant contribution in unraveling this argument.

The one-step energy release rate is given by

$$\rho q_c A \exp\left[-\frac{E_a}{\tilde{R}T}\right] \ . \tag{3.63}$$

Figure 3.19 shows the heat-loss rate, the heat-release rate, and temperature as a fluid element, initially outside the boundary layer ($x_0 = 0.01$ m, $y_0 = 0.01$ m, Trajectory 1 in Figure 3.20), is entrained by the boundary and heated. The point of ignition is defined as the point where the heat-release rate and heat-loss rate are equal. Several of these trajectories are shown in Figure 3.20, which demonstrate how the ignition location changes with the initial location. For Trajectory 3, for example, the temperature gradients in the boundary layer are higher and thus the heat diffusion is higher, which leads to the fluid element ignition closer to the hot surface.

If we consider the case where the density is variable the effect will be a stretching of the solution as described in Equation 3.29, the detailed calculation has been done by Cairnie and Harrison (1982). For the trajectories considered, this implies that the paths are shifted away from the wall. However, since both the temperature and velocity profile are shifted away from the wall, the final dominant balance arguments laid forth are still valid and the qualitative features of ignition should be predicted correctly in the same manner as presented above, although the precise ignition location will be incorrect. A more realistic simulation would require considering the full two-dimensional solution and a detailed chemical reaction mechanism, but this is outside the scope of this thesis.

It should be noted that ignition occurs fairly far away from the wall in Figure 3.20. This is due to the fact that the wall temperature was too high in this example. A more rigorous study would require varying the temperature and using non-averaged fluid properties. However, this is also outside the scope of this thesis.

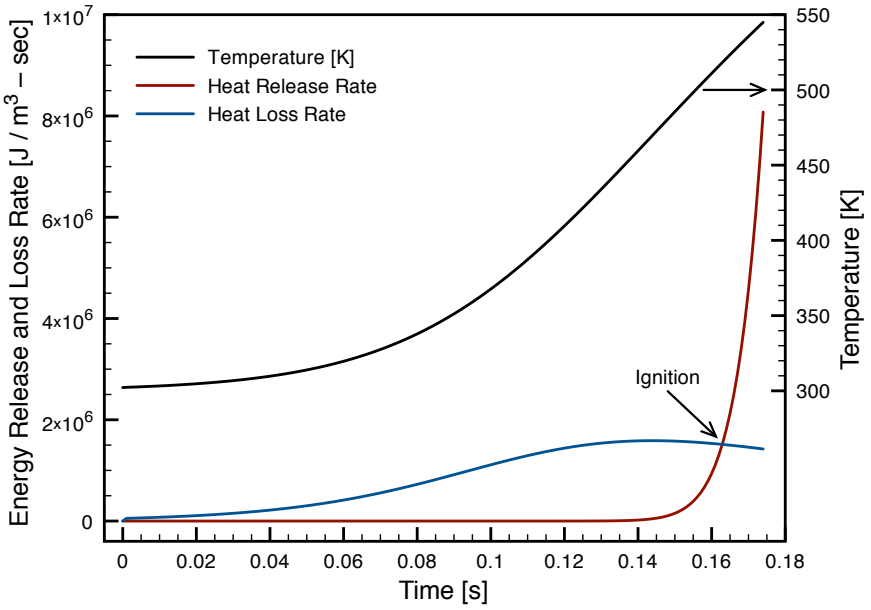

Figure 3.19: Energy release rate, energy loss rate, and temperature along a fluid trajectory ($x_0 = 0.01$ m, $y_0 = 0.01$ m); the ignition location is indicated as the point where energy loss rate equals the energy release rate

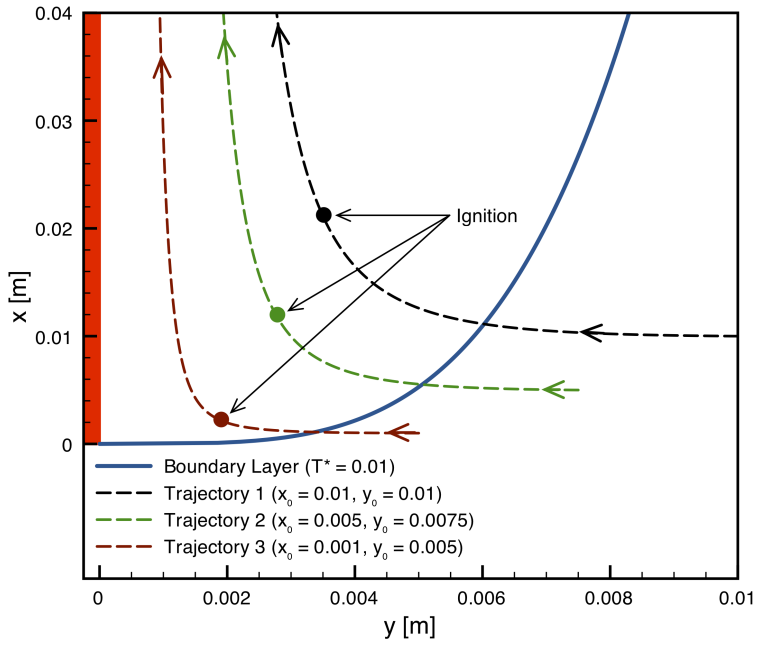

Figure 3.20: Trajectories of fluid elements into a boundary layer created by a hot surface at the left edge; the ignition location is defined as the point where energy release rate equals the energy loss rate

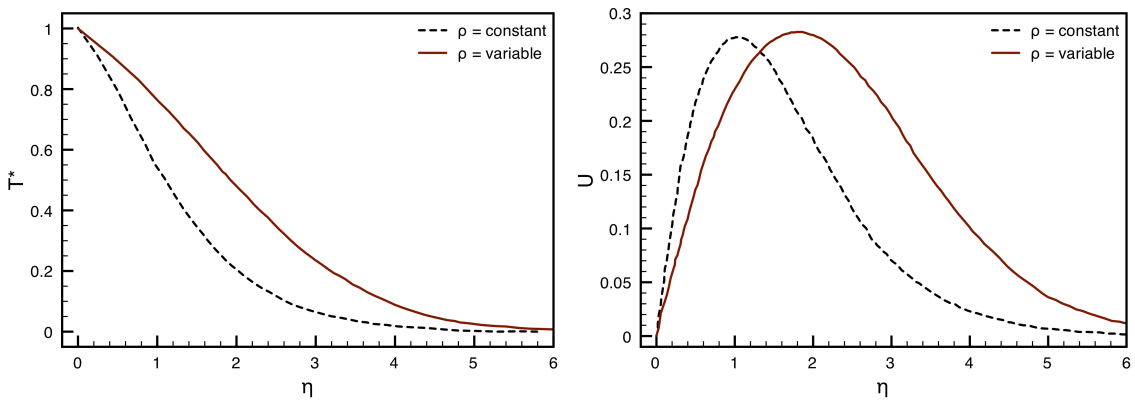

(a) (b)

Figure 3.21: Nondimensional (a) temperature profile and (b) velocity profile for a constant and variable density boundary layer along a vertical hot plate (from Cairnie and Harrison, 1982) (T_w/T_∞ ~2.3 – $T_w \sim 690$ K, $T_\infty \sim 300$ K)

3.4.3.1 Thermal Ignition Using Tabulated and Detailed Chemistry Modeling [3]

The final approach taken in investigating hot surface ignition is the numerical simulations of the fluid dynamic processes (convection and diffusion) in conjunction with finite rate chemistry. The hot surface temperature leading to ignition of various flammable mixtures is investigated.

This work utilizes a detailed reaction mechanism for heavy hydrocarbon fuels which has been validated extensively over a wide range of temperatures, pressures, and equivalence ratios (Blanquart et al., 2009, Narayanaswamy et al., 2010). Although the fuel used in the experiments is hexane, the simulations were performed using n-heptane. This is because the chemistry of heptane at low temperatures is better understood than that of hexane; more experimental data exist for heptane to validate the chemical model; and previous studies have shown that normal alkanes have very similar ignition and flame propagation characteristics (Davis and Law, 1998a, Shen et al., 2009, Westbrook et al., 2009).

Simulation Details Simulations are carried out in a 2D axisymmetric domain with the symmetry plane established at the center line of the cylinder, which is assigned a Neumann boundary condition, while all the other surfaces except the glow plug are modeled as closed adiabatic walls.

The experimental observations indicated that the surface temperature of the glow plug is almost uniform. As a result, in the simulations, the glow plug is initialized spatially with a uniform tem-

[3]Portions of the following work were submitted but not accepted to 34$^{\text{th}}$ Combustion Symposium in the paper "Investigation of hot surface ignition of a flammable mixture" by S. Menon, P. Boettcher, B. Ventura, J. Shepherd, G. Blanquart.

perature. Furthermore, the temperature of the glow plug is kept fixed in time, rather than being increased up to a final value as in the experiments.

The progress variable at the glow plug surface is set to zero. A zero value for the progress variable at the wall can be understood in two different ways. First, it means that no increase in temperature is allowed above the imposed, unburned temperature (T_u). Second, it is representative of the destruction of radicals at the wall through their recombination into stable species. The surface itself is inert having no chemical reactions with the mixture. The sensitivity of the simulation results to this boundary condition is checked by using a Neumann boundary condition at the glow plug surface. The results indicates no change in the ignition location or delay time.

The solution is obtained on a mesh consisting of 256 grid points in the vertical direction and 128 points in the radial (horizontal) direction. The grid is clustered closer to the glow plug with 128 points for one glow plug height and 32 points for one glow plug diameter. Simulations are performed using the NGA code (Desjardins et al., 2008). The code relies on high order conservative finite difference schemes developed for the simulation of variable density flows. A third order WENO scheme is used to compute scalar transport (Liu et al., 1994).

Figure 3.22 shows contours of the progress variable at the time of ignition corresponding to different hot surface temperatures. Figure 3.22 (a) and (b) correspond to simulations performed with the full chemical model, including low temperature reaction pathways. Figure 3.22 and (d) correspond to simulations performed without the low temperature reaction pathways. The ignition kernel is illustrated by the black iso-contour.

The numerical simulations predict that ignition occurs above the glow plug surface, consistent with experimental observations. The location of ignition is found to be insensitive to the surface temperature when only the high-temperature chemistry is considered. However, when the full model is used, the ignition location depends on the surface temperature and decreases in height with increase in surface temperature (Figures 3.22 (a) and (b)). Additionally, the minimum surface temperature required to ignite the mixture decreases when the full model is used.

Figure 3.23 shows the effect of mixture equivalence ratio on the minimum temperature for ignition. The experimental results are the same as presented in Figure 3.15, however, only the minimum value corresponding to a particular equivalence ratio is included. For each equivalence ratio the hot surface temperature is varied until ignition is no longer observed. Lack of ignition is indicated by an asymptotic behavior for the maximum value of the progress variable in the domain.

The ignition temperature (around 920K) obtained from experiments, appears to be fairly inde-

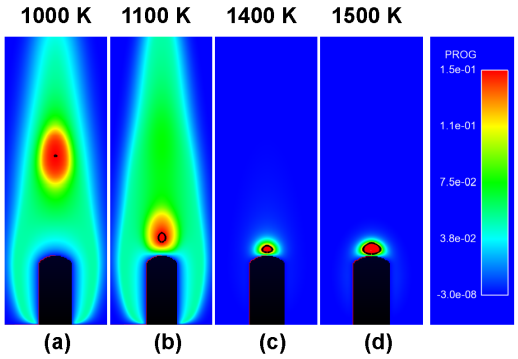

Figure 3.22: Comparison of ignition locations for different hot surface temperatures; the full chemical reaction mechanism is considered in (a) and (b), while the low temperature reaction pathways are neglected in (c) and (d)

pendent of the equivalence ratio. A similar behavior, at higher temperature (T $\approx$ 1400K) is observed for the simulation where low temperature (LT) chemistry is excluded. However, when the full chemical model is used, the simulation results in Figure 3.23 show a considerable effect of equivalence ratio on minimum hot surface temperature for ignition and lead to values that are smaller than that measured experimentally.

While the chemical model gives very good results for low temperature ignition under high pressures, it remains unvalidated for atmospheric pressures. The present results may suggest that the low temperature chemistry is too fast for rich conditions. Despite uncertainties in the low temperature pathways, the simulations confirm that a mixture with an equivalence ratio less than 0.5 should not ignite.

The deviation from experimental results seem to be in part due to our incomplete understanding of the low temperature reaction kinetics and indicates an area of future research.

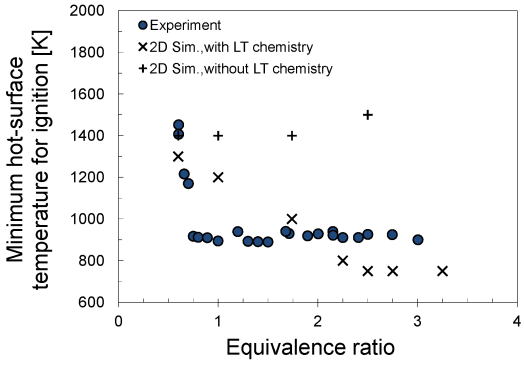

Figure 3.23: Hot surface ignition temperature from tabulated chemistry simulations (with and without low temperature, LT, chemistry) and experiments

3.4.4 Hot Surface Ignition Temperature as a Function of Pressure

The pressure dependence of the ignition temperature is investigated for two cases while holding the equivalence ratio constant in the range of total pressure from 25 kPa to 100 kPa. Experimental results in Figure 3.24 show that the required ignition temperature increases as the pressure is decreased.

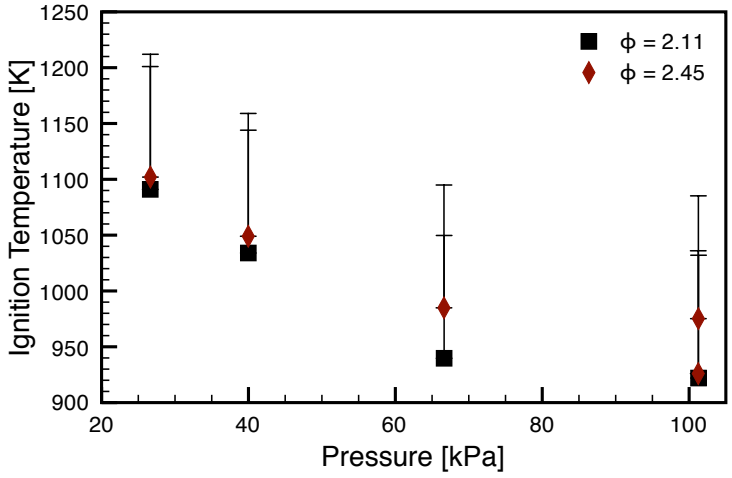

Figure 3.24: Ignition delay times for n-heptane and air mixtures computed with the detailed chemical mechanism of Curran et al. (1998)

We can apply the model of equating the thermal diffusion time scale to the ignition time scale to estimate the pressure dependence by calculating the ignition time as a function of pressure. The thermal diffusion time computed from Equation 3.47 remains basically unchanged as the pressure is changed from 100 kPa to 25 kPa. Figure 3.25 shows both the temperature calculated leading to ignition in 250 ms, the ignition temperature, as well as the ignition time at a constant temperature, 1000 K, computed using the chemical mechanism from Curran et al. (1998) in a isobaric calculation with varying initial pressure[4]. At both equivalence ratios tested an increase in ignition temperature with a decrease in pressure is observed.

As in the previous section, the results presented here depend on the size of the hot surface element. The particular fluid element trajectory as well as the time spend near the hot surface greatly influence the temperature and reaction history. For a quantitative prediction of the ignition temperature, it is necessary to solve the nonsteady evolution of the hot surface temperature, the detailed chemical processes, thermal and species diffusion along with the fluid mechanics, and surface reactions. As shown in the previous chapter, this is a difficult task even in zero-dimensional calculation.

[4]The author would like to thank Guillaume Blanquart for performing these simulations.

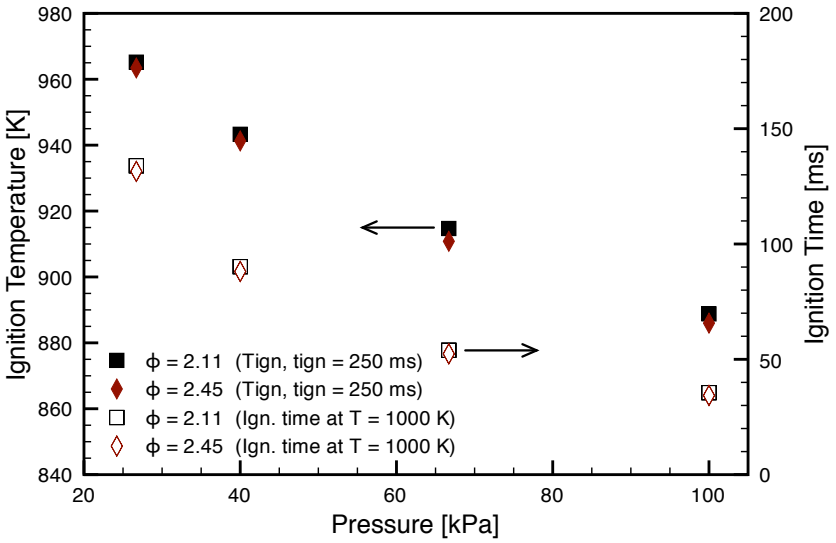

Figure 3.25: Simulated ignition temperatures and ignition times as function of pressure

3.4.5 Hot Surface Ignition Temperature as a Function of Surface Area

The ignition temperature is observed to be correlated with the the hot surface size and shape (Kuchta et al., 1965, Laurendeau, 1982), neglecting any additional effect that catalytic properties of the hot surface that may be present. Semenov (1940) made some analytical progress, described in Appendix E, arriving at the following relationship for the ignition temperature, T_1 as a function of radius for heated wires of radius, r, in a vessel of a specified radius, R_V, kept a constant temperature, T_0,

$$r \ln \frac{R_V}{r} = \left(\frac{E_a \lambda \left(T_1 - T_0\right)^2}{2 R_V T_1^2 Q A \exp\left[-E_a/(\tilde{R} T_1)\right]} \right)^{1/2} . \tag{3.64}$$

This is based on a one-step chemical reaction model, where the reaction energy, Q, is released according to Arrhenius rate described by the activation energy, E_a, and pre-exponential, A. Kuchta et al. (1965) simplified this relationship by assuming that the exponential term dominates, expanding the left-hand side, and keeping only the leading order term,

$$r \sim \exp\left[E_a/(2\tilde{R} T_1)\right] . \tag{3.65}$$

Taking the natural logarithm of both sides yields the approximate $T \sim [\ln r]^{-1}$ dependence of the ignition temperature on surface area:

$$\ln r \sim \frac{1}{T_1} . \tag{3.66}$$

The experimental data presented by Kuchta et al. (1965) support this scaling analysis (see Figure 3.26) over a range of hot surface sizes between 0.6 cm^2 and 70 cm^2. Based on our experiments we found ignition temperatures of up to 300 °C lower at a surface area of about 1.5 cm^2 and thus we strongly caution against extrapolation of the Kuchta et al. (1965) results when making safety assessments.

Kuchta et al. (1965) show ignition temperatures for heat sources of comparable surface area to that of the glow plug (0.63 cm^2) to be 1270 K. When compared using the radius of the glow plug (0.165 cm), temperatures were observed to be 1070 K (Kuchta et al., 1965). These values were obtained using heated wires and rods in a 400 cm^3 vessel maintained at 150 °C. The test gas was passed through the reactor at 0.35 cm/s calculated from the volumetric flow rate. In contrast, the vessel wall in the current experiment remained at room temperature and the characteristic flow velocity in the plume above the glow plug is 40 cm/s based on simulation results. Smyth and Bryner (1997) performed experiments with a combustible mixture impinging on hot metal surfaces made from nickel, stainless steel, and titanium at 45° at a flow speed of 16 cm/s. The overall average ignition temperature for n-hexane was 1105 K. Both of these previous studies were performed in open combustion vessels, which is similar to the technique employed in the standard for auto-ignition temperature testing (ASTM, 2005), which limits the accuracy of the composition control.

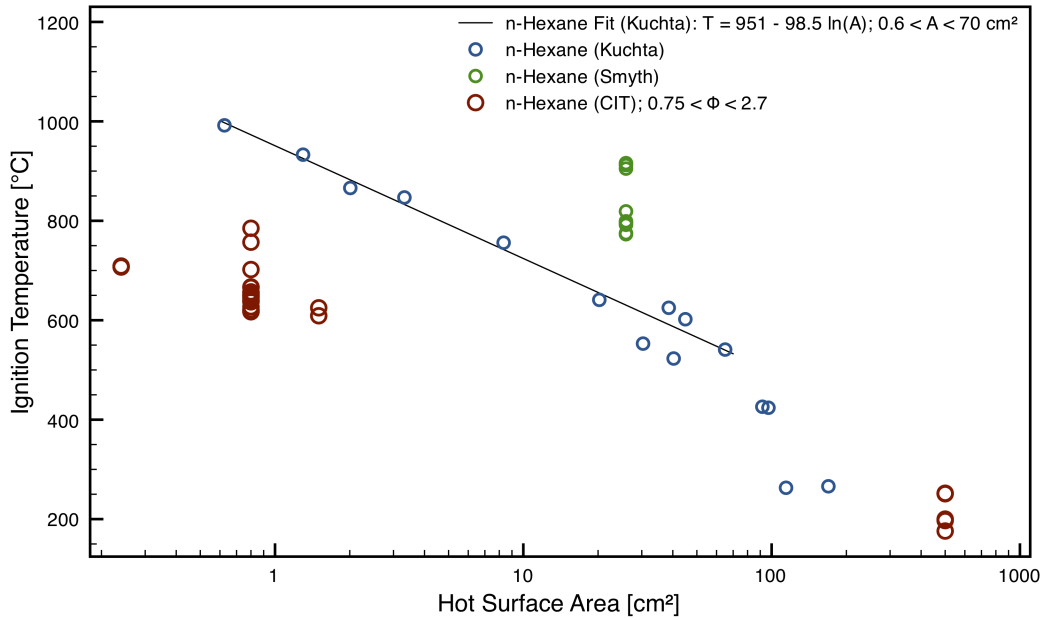

Figure 3.26: Ignition as a function of hot surface size (uncertainty in ignition temperature for CIT measurements is +110 K). Range in values for CIT measurements is due to a range of compositions and initial pressure.

Figure 3.26 demonstrates the overall trend in which the ignition temperature increases with decreasing hot surface area. The large range in ignition temperatures in the current data are due to the range of equivalence ratios examined examined in the present study. The higher flow velocity of Smyth and Bryner (1997) leads to an increase in the ignition temperature relative to the Kuchta et al. (1965) data. The logarithmic curve fit of the historical data greatly underestimates the minimum ignition temperatures observed in the current study.

The ignition temperature data includes the auto-ignition experiments presented in the previous chapter on the far right of Figure 3.26. These ignition temperatures also fall below the historical values because they were performed in a closed vessel initially at room temperature and heated to the ignition temperature, rather than introducing the fuel at atmospheric pressure.

3.5 Flame Propagation

In our studies, we found three different flame regimes, single, multiple ignitions, and puffing flames, which are continuous flames with large scale instabilities. The flame propagation is discussed in this section and puffing flames are detailed in the next chapter. A schlieren system was used in order to confirm that ignition of the mixture occurred. In addition to determining if and where ignition had taken place, the schlieren movie can be used to observe the flame propagation, determine the flame speed, and observe instabilities. While the experiment is not specifically designed to determine laminar flame speeds, the observations can be compared to literature data and simulations by making reasonable assumptions about the gas motion.

3.5.1 Experiments

The schlieren system records gradients in image intensity corresponding to density gradients, which are very prominent across the flame front ($\rho_{\text{unburnt}}/\rho_{\text{burnt}} \sim 5.5$–$8$). Experiments used a 150 W Oriel Arc Light Source (P/N 66907), which is focused on a pinhole and then collimated using a 1.5 m focusing mirror. Best results were obtained when using a transparency with a small circular black spot as the schlieren stop (dark background schlieren). Figure 3.27 shows a dark background schlieren image, which has clear outlines of the flame shape for all flame orientations. The image was captured using a Phantom v710 high-speed camera using a resolution of 800×800 pixels with frame rates of 1000–2000 fps and exposure times of 5–50 μs.

The flame position is digitized using a Matlab digitizing routine[5], which manually measures the position of the flame relative to the top of the glow plug (origin). For the left and right flame positions, the horizontal distance between the left most edge and right most edge and origin are used. The diameter of the window visible in the image is used as the reference length scale.

Representative results of the digitized flame position as a function of time are shown in Figure 3.28. The initial slope is higher than the final value due to the increased gas temperature in the plume as well as the curvature effects on the flame propagation. The start of the linear regime is found by inspection of the raw data and the final propagation speed is computed by linear least squares regression of the data in the linear regime.

[5]The digitizing routine used here is based on the digitize.m program written by J. D. Cogdell and the digitize2.m program written by A. Prasad, both available from the Mathworks File Exchange with edits from M. Rubel and J. S. Damazo. Both programs have been invaluable tools in preparing this thesis.

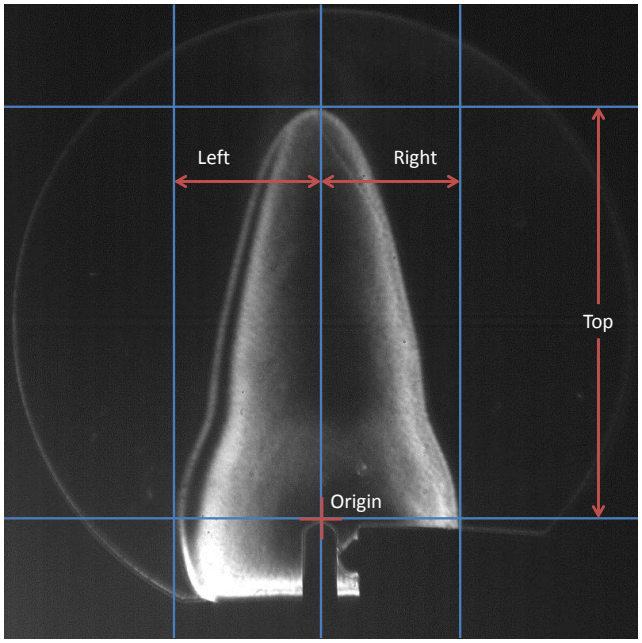

Figure 3.27: Definition of flame outside and origin location

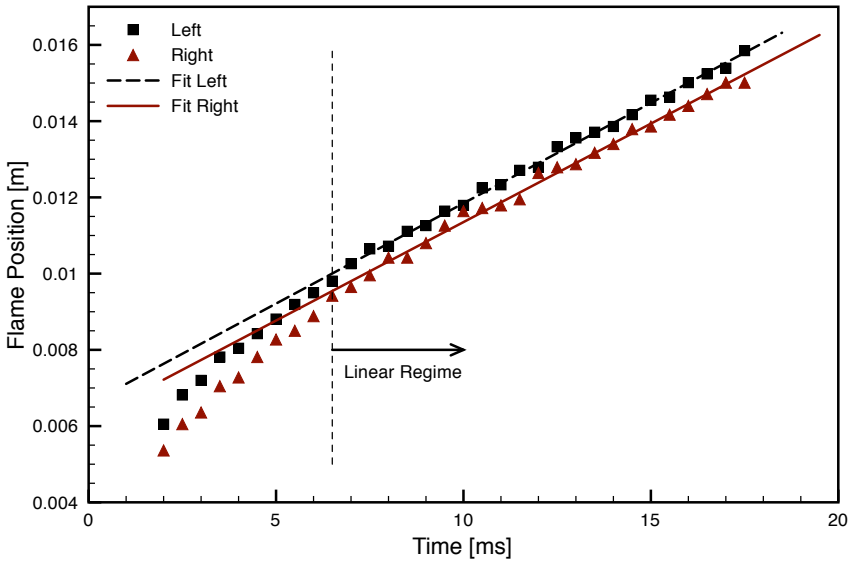

Figure 3.28: Representative digitization of the flame location and fit flame speed from shot 33

3.5.2 Flame Propagation Speed as a Function of Composition

The composition, initial pressure and temperature of the flammable mixture are significant factors in determining the propagation speed of the flame (Glassman, 2008). Several methods are available to measure this dependence, including closed combustion vessels (Kelley et al., 2011), and counterflow burners (Ji et al., 2010), and the laminar unstretched burning velocity S_L is reported. Detailed data from the literature for n-hexane and n-heptane is given in Appendix F and compared to the present experimental results. Due to the less than ideal conditions of the current setup for measuring flame speed, we can only make an approximate comparison to the literature value as the effects of flame stretch and strain, flow out in front of the flame, and heat transfer during the flame propagation are not taken into account.

As a first idea, we idealize the flame as sphere, and compute the propagation speed, $\dot{R}$, as the sum of the flame propagation speed and the flow speed, u, established by the expansion of the hot gas inside the flame. In order to carry out this computation, we assume that the gas inside the flame is stationary. Detailed simulations, discussed later, show that this is not the case, but that the error introduced is acceptable.

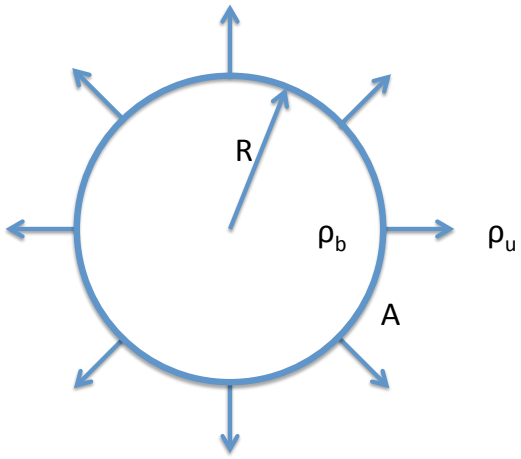

Figure 3.29: Spherical flame schematic

Another method is to use conservation of mass. The mass flux of burned gas into the flame, $\dot{m}_b$, is equal to equal to the mass flux of unburned gas through the flame front, $\dot{m}_u$,

$$\dot{m}_b = \rho_b \dot{V} = \rho_b 4\pi R^2 \dot{R} \tag{3.67}$$

$$\dot{m}_u = \rho_u S_L A = \rho_u S_L 4\pi R^2 \tag{3.68}$$

$$\dot{m}_u = \dot{m}_b \Longrightarrow \dot{R} = \frac{\rho_u}{\rho_b} S_L = \epsilon S_L \tag{3.69}$$

where ϵ is the expansion ratio, ρ_u/ρ_b, Equation 3.69 gives an approximate flame propagation speed as laminar burning velocity given in the literature times the expansion ration, which can be computed from a constant pressure equilibrium calculation.

Alternatively, we can approximate the lower part of the flame as an expanding cylindrical flame with inflow at the top. This is can be accomplished by considering the incompressible flow just inside the flame.

$$\nabla \cdot \vec{u} = 0 \tag{3.70}$$

From simulations of stoichiometric fuel-air mixtures, the mass inflow at the top can be approximated by a top hat profile with an inflow velocity, u_z, of 2 m/s over a radius of 2 cm, R_1. At a point in time where the flame is about 6 cm, R_2, in diameter and 2 cm high, h, the outflow velocity, u_r^- just behind the flame front can be calculated

$$\int \vec{u} \cdot \hat{n} dA = 0 \tag{3.71}$$

$$\int_0^{R_1} u_z 2\pi r dr = \int_0^h u_r^- 2\pi R_2 dz \tag{3.72}$$

$$u_r^- = \frac{u_z R_1}{2R_2 h} \tag{3.73}$$

The outflow at the flame front, u_r^-, is about 10 cm/s, which is small relative to the measured flame velocities, V_f. The flame propagation velocity is the sum burning speed and the underlying flow velocity,

$$V_f = S_l + u_r \ . \tag{3.74}$$

The effect of the outflow is small except at very large equivalence ratios, where the shape of the flame is drastically influenced by the fluid motion. Consequently, for comparisons of the flame propagation speed with literature values the spherical approximation is reasonable.

The experimental flame propagation speed at the left side, right side, and top are given in Figure 3.30. The vertical burning velocity is clearly influenced by both the flow in the plume

above the glow plug and the increased temperature in this region, which is discussed in detail in Section 3.5.4.

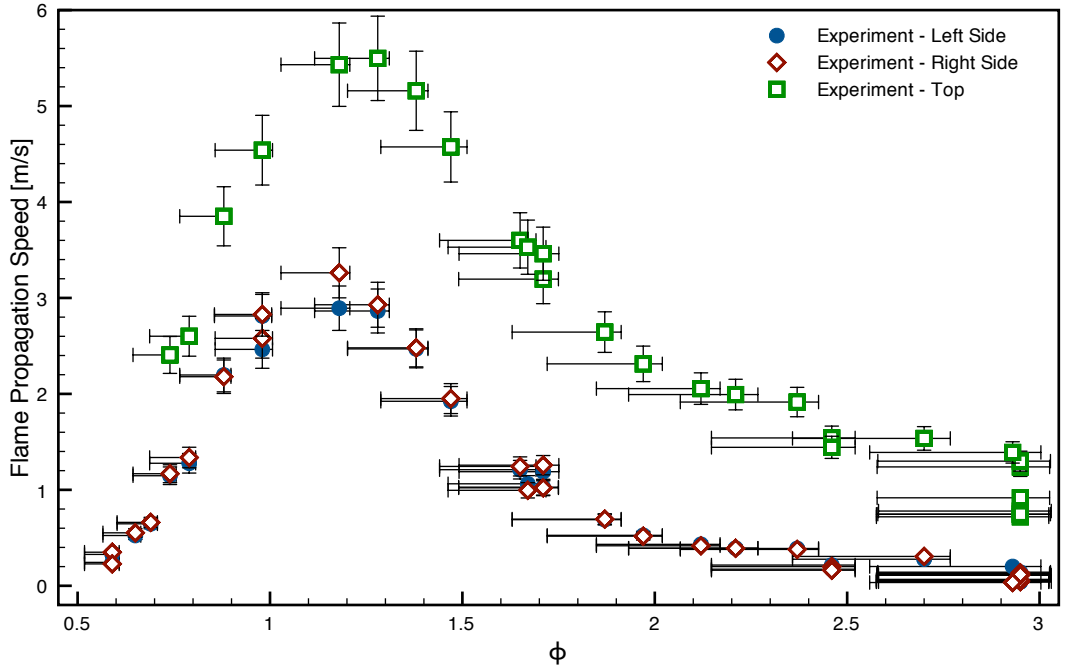

Figure 3.30: Flame propagation speed for n-hexane air mixtures as a function of equivalence ratio at atmospheric pressure

The measurement uncertainty that arises include the measurements of the reference scale, the window size, aberrations due collimation errors, and uncertainty in the position of the flame front . All of these errors result in a total of 8% uncertainty in the flame propagation speed. More rigorous experiments have been performed by Mével et al. (2009) to determine flame speeds in spherical pressure vessels and found uncertainties of 6%. Given the complicated flame shape arising from plume temperature distribution the larger uncertainties in our experiment are not unreasonable.

3.5.3 Computational Modeling of Flame Propagation [6]

The governing equations of fluid motion for the simulations performed here are the variable density, low-Mach, number Navier-Stokes equations.

$$\partial_t \rho + \nabla \cdot (\rho u) = 0 \tag{3.75}$$

$$\partial_t (\rho u) + \nabla \cdot (\rho u u) = -\nabla p + \nabla \cdot \tau + \rho g \tag{3.76}$$

where τ is the viscous shear stress tensor and g represents the gravity vector.

The simulations are performed using the NGA code (Desjardins et al., 2008). The code relies on high order conservative finite difference schemes developed for the simulation of variable density turbulent flows.

The closed vessel is modeled as a sufficiently large volume. The symmetry of the problem allows the computation to be performed on a 2D axisymmetric structured mesh. The mesh is locally refined in the vicinity of the glow plug in the horizontal and vertical directions. A Dirichlet boundary condition consisting of a temperature profile is assigned to the glow plug surface. The temperature at any location on the glow plug is constant in time but it varies in space along the surface of the glow plug to match experimentally determined values. The walls of the vessel are modeled as adiabatic boundaries.

The code utilizes a lookup table procedure to acquire species and mixture properties during the course of the simulation. Two elements critical in reproducing the experimental results are the chemistry tabulation and the reaction mechanism.

3.5.3.1 Chemistry Tabulation

Reaction chemistry is incorporated using a lookup table procedure where species and mixture properties are tabulated as a function of the unburned gas temperature (T_u) and the progress variable (C). The code utilizes the flamelet progress variable (FPV) approach, which requires the solution of transport equations for additional scalar variables, namely,the progress variable,

$$\partial_t (\rho C) + \nabla \cdot (\rho u C) = \nabla \cdot (\rho D \nabla C) + \dot{\omega}_C \tag{3.77}$$

[6] The numerical simulations were performed by Shyam K. Menon and Guillaume Blanquart using geometries and temperature distribution from the experimental setup.

and the transport of the unburned gas temperature

$$C_{p,u}\left[\partial_t(\rho T_u) + \nabla \cdot (\rho u T_u)\right] = \nabla \cdot [\lambda \nabla T_u] \tag{3.78}$$

The progress variable is defined to be the sum of mass fractions of major product species — CO, CO_2, H_2 and H_2O, and is used to represent the extent (or progress) of the reaction.

The transport equation for temperature relates to the unburned gas and hence it does not have any chemical source terms in it. The approach pursued here currently uses unburned gas temperature in-lieu of enthalpy. Since there are no other energy loss or source terms being considered in the current simulation, the two variables (temperature and enthalpy) are equivalent. Species mass fractions, production rates, mixture transport properties, flame speeds etc., are tabulated as a function of the unburned gas temperature and reaction progress variable. Prior to tabulation, these properties are obtained from calculations for freely propagating laminar premixed flames conducted with full detailed chemistry using the FlameMaster software (Pitsch and Bollig, 1994).

3.5.3.2 Reaction Mechanism

For 1-D flat flames at constant unburned gas temperature (T_u), the model reproduces the laminar flame speeds from kinetic models. Hence, the accuracy of the 2-D axisymmetric simulations is limited by the accuracy of the kinetic model.

The reaction mechanism used in this work is one for heavy hydrocarbon fuels which been extensively validated over a wide range of temperatures, pressures, and equivalence ratios (Blanquart et al., 2009, Narayanaswamy et al., 2010). Heptane is used as the fuel in all simulations since the reaction model is calibrated against numerous heptane experiments. Previous studies have shown that normal alkanes show very similar ignition and flame propagation characteristics (Davis and Law, 1998a, Shen et al., 2009, Westbrook et al., 2009) so we expect that the results will be comparable to hexane.

The detailed mechanism is used to estimate flame speeds for *n*-heptane-air mixtures at different equivalence ratios and unburned gas temperatures at which experimental data are available from literature Davis and Law (1998b); Huang et al. (2004); Kumar et al. (2007); Ji et al. (2010); Kelley et al. (2011); and Van Lipzig et al. (2011). The calculations are carried out using FlameMaster and results are shown in Figure 3.34. The detailed chemical model is able to predict the effects of unburned temperatures and equivalence ratios on the burning velocity. The agreement between simulation and experimental results give us confidence in the model.

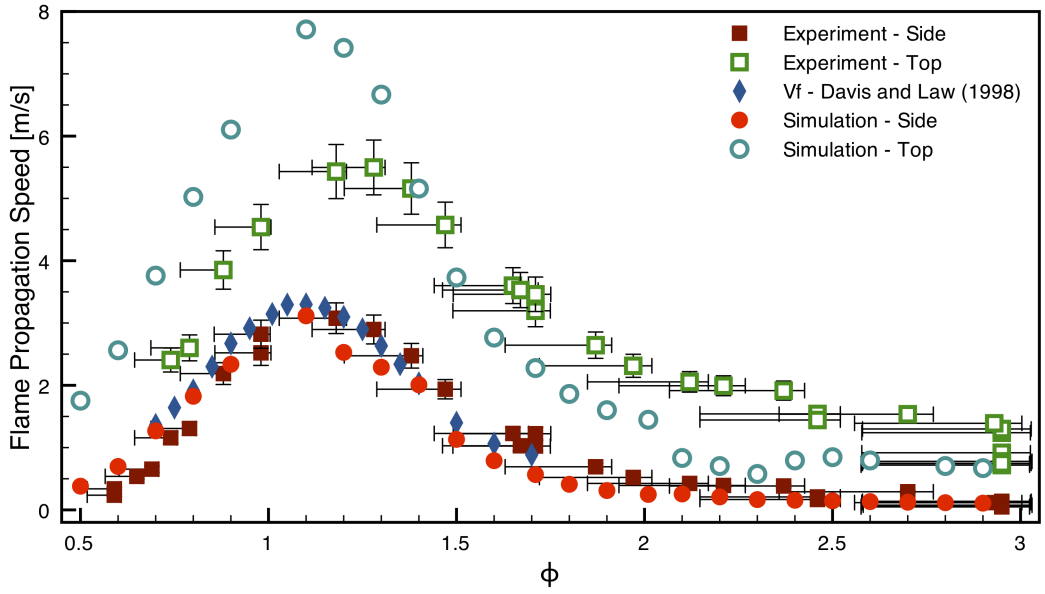

Figure 3.31: Flame propagation speed at room temperature and atmospheric pressure including the estimated flame propagation speed from Davis and Law (1998b) calculated by multiplying the the laminar burning velocity by the expansion ratio obtained by equilibrating the mixture at constant pressure using the reduced Ramirez mechanism (Ramirez et al., 2011)

The overall shape of the flame is well captured in the numerical simulation as shown in Figures 3.32 and 3.33. As for the experiment, the flame propagation speed in the simulation is determined by tracking the flame edges as shown in Figure 3.27. Figure 3.31 gives a detailed comparison of the flame propagation speed obtained in the simulation and the experiments. The agreement is reasonable and consistent with the estimated uncertainties in the measure flame speed and composition. The discrepancy between the simulation and experiments ranges from 0.15 to 0.8 m/s with an average of 0.46 m/s. The flame propagation speeds at the top have a larger discrepancy between the experiments and simulations, which may be attributed to the uncertainties in the plume temperature, and the fact that the plume temperature is transient in the experiment and steady-state in the simulations.

The simulation results have several sources of uncertainty and error including a lack of validation of the chemical mechanism for $\phi > 1.7$, for no laminar flame speed data is available. Additionally, the flamelet model introduces unquantified uncertainties and the location of the flame is a function of the progress variable value chosen.

The shape of the plume as indicated by the density of the gas mixture in the (first frame of Figure 3.33) is in qualitative agreement with that shown in the schlieren images taken in the experiments (first frame of Figure 3.32).

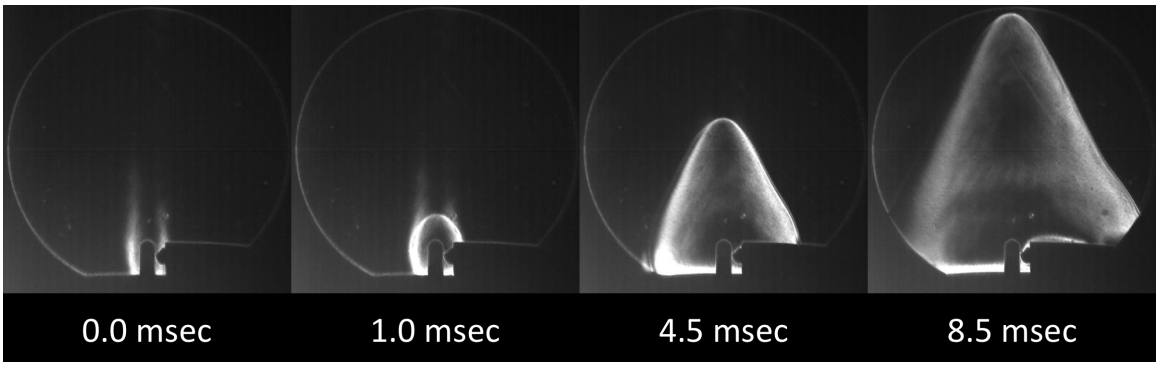

Figure 3.32: Dark background schlieren visualization of the flame propagation for a hexane-air mixture (Bosch glow plug, $\phi = 1.2$)

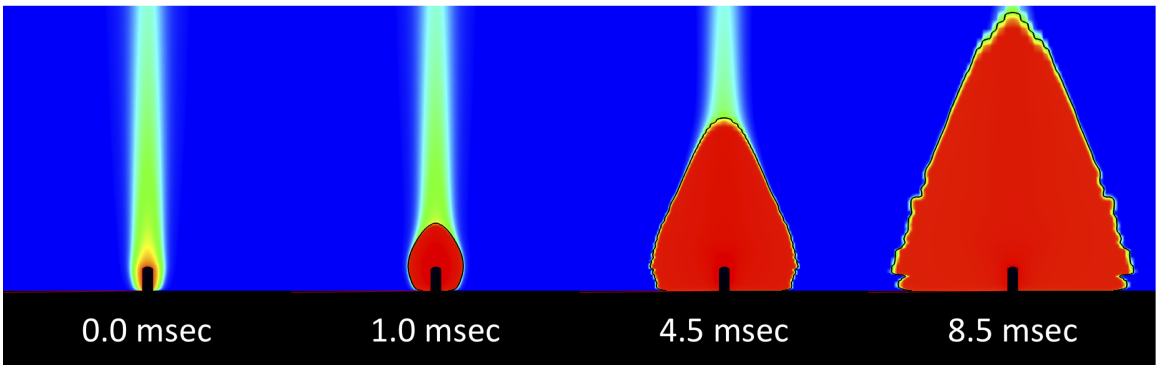

Figure 3.33: Simulation results for flame propagation phenomena (Bosch glow plug, $\phi = 1.2$)

3.5.4 Effect of the Thermal Plume on the Flame Propagation Speed

As seen above the the flame propagation speed is different at the top of the flame and on the sides. The major contributing factor to this phenomenon is the elevated temperature in the plume above the glow plug. Some scaling arguments about the size and temperature in the plume are given in Appendix G.

The effect of temperature on flame propagation speed has been investigated by experimentally by Davis and Law (1998b), Huang et al. (2004), Kumar et al. (2007), Ji et al. (2010), Kelley et al. (2011), and Van Lipzig et al. (2011). Results of simulations based on Blanquart's CaltechMech reaction mechanism (Blanquart, 2011) are shown in Figure 3.34. The simulation reproduces the observed temperature dependence and experimental data. Figure 3.35 illustrates that even a temperature increase of 100 K can raise the laminar flame speed by over 50%. Although data are not available at the highest temperatures observed in the plume, the extrapolation of the flame speed shown in Figure 3.36 indicates that the flame speeds could be as high as 200-300 cm/s immediately above the glow plug (Gaydon and Wolfhard, 1979).

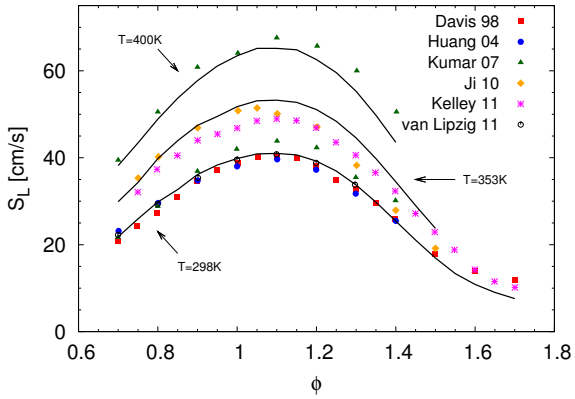

Figure 3.34: Laminar burning speed as function of equivalence ratio at different temperatures as calculated using the CaltechMech

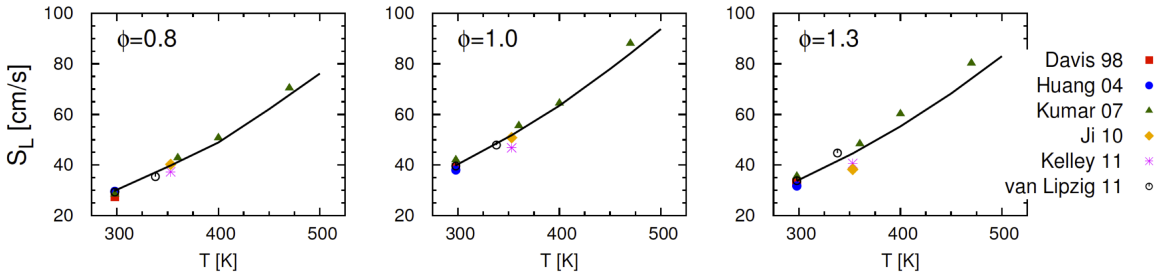

Figure 3.35: Comparison between laminar burning speeds calculated using n-heptane-air reaction mechanism and experimental data by Davis and Law (1998b), Huang et al. (2004), Kumar et al. (2007), Ji et al. (2010), Kelley et al. (2011), and Van Lipzig et al. (2011)

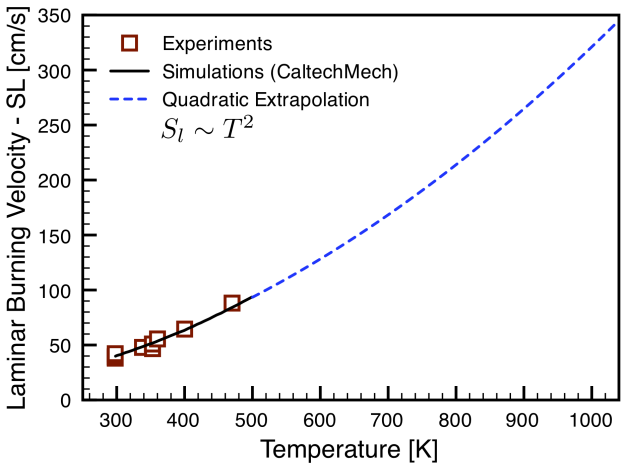

Figure 3.36: Laminar burning velocity of stoichiometric n-heptane as a function of temperature as found in experiments, predicted by the CaltechMech (Blanquart, 2011), and quadratic extrapolation of the simulation results ($\phi = 1.0$)

In order to make accurate comparisons with simulations, it is necessary to make measurements of the temperature in the plume in order to calibrate the nonreactive plume model. An array of thermocouples[7] was placed directly above the glow plug as shown in Figure 3.37. The thermocouples are spaced vertically approximately 1 cm apart along the centerline.

For comparisons of the initial conditions of the experiment with the simulations, the temperature in the plume is measured with air in the vessel as shown in Figure 3.38 (a). The glow plug is powered on at ∼1 second raising its temperature as well as the plume temperature and then turned off at ∼10.5 seconds allowing it cool off. The array was also in place during an ignition and flame propagation experiment shown in Figure 3.38 (b), but due to the limited time response it is not possible to use these results to estimate the flame speed or temperature.

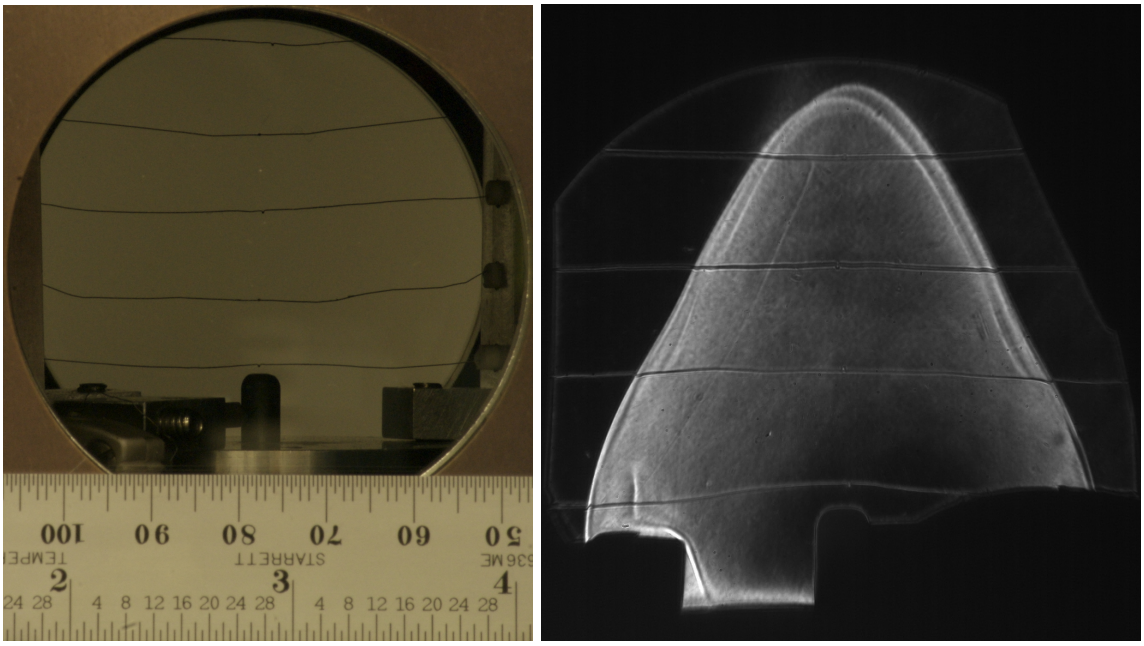

(a) (b)

Figure 3.37: (a) Picture of the thermocouple array in the vessel used to determine the plume temperature; (b) schlieren image during shot 61 with the thermocouple array in place

The simulation of the plume temperature is performed for the Autolite glow plug at 1320 K, which corresponds to the peak temperatures in Figure 3.38 (a). The simulation, like the experiment, is performed without chemical heat-release. The results, given in Figure 3.39, indicate reasonable agreement between the simulation and experiment.

It should be noted that the maximum temperatures observed by the thermocouple in Figure 3.38 (b) are significantly below the adiabatic flame temperature, which is around 2200 K for hydrocarbon

[7]The thermocouple array was designed and implemented by Brian Ventura.

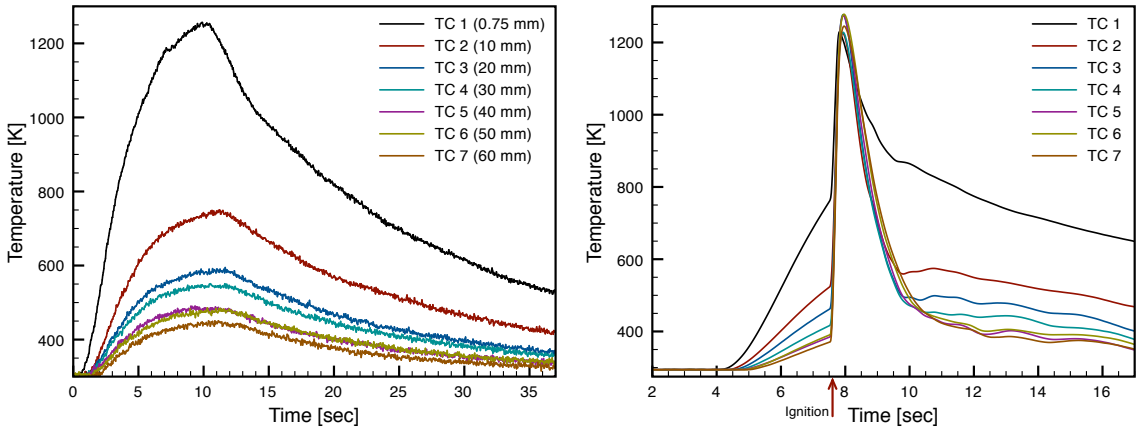

(a) (b)

Figure 3.38: (a) Temperature distribution above the glow plug without ignition from thermocouple array; (b) temperature distribution above the glow plug with ignition during shot 61 ($\phi = 1.0$ hexane-air mixture, ignition occurred at 7.0645 s as indicated on the x-axis)

combustion in air (Glassman, 2008). This experiment was not designed to measure adiabatic flame temperatures. As the flame passes over the thermocouples, the response time of the thermocouple creates a lag during which the temperature decreases and additionally the thermocouple losses heat to conduction along the wires as well as radiation.

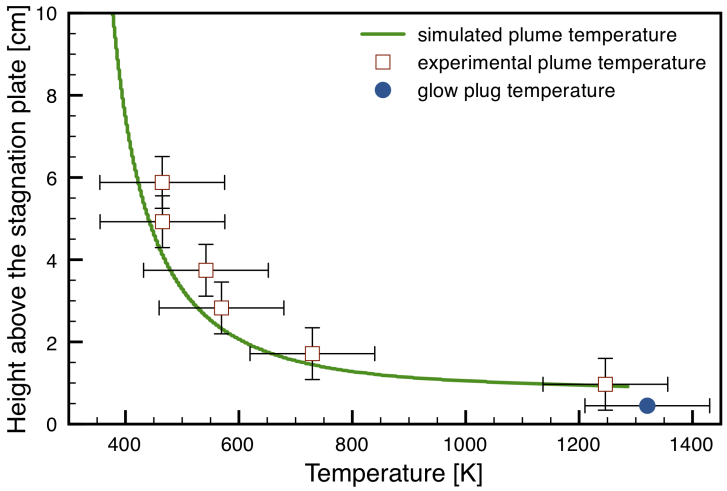

Figure 3.39: Temperature distribution in air above the glow plug comparing simulations and thermocouple measurements

3.5.5 Combustion Modes

The experiments show three different combustion modes depending on the composition and initial pressure. The first mode involves a single flame propagating until it reaches the vessel walls as shown in the sequence of images from a schlieren video in Figure 3.40. In the second mode, two to three flames ignite sequentially, as shown in Figure 3.41. The final mode corresponds to a continuously puffing flame, as shown in Figure 3.42.

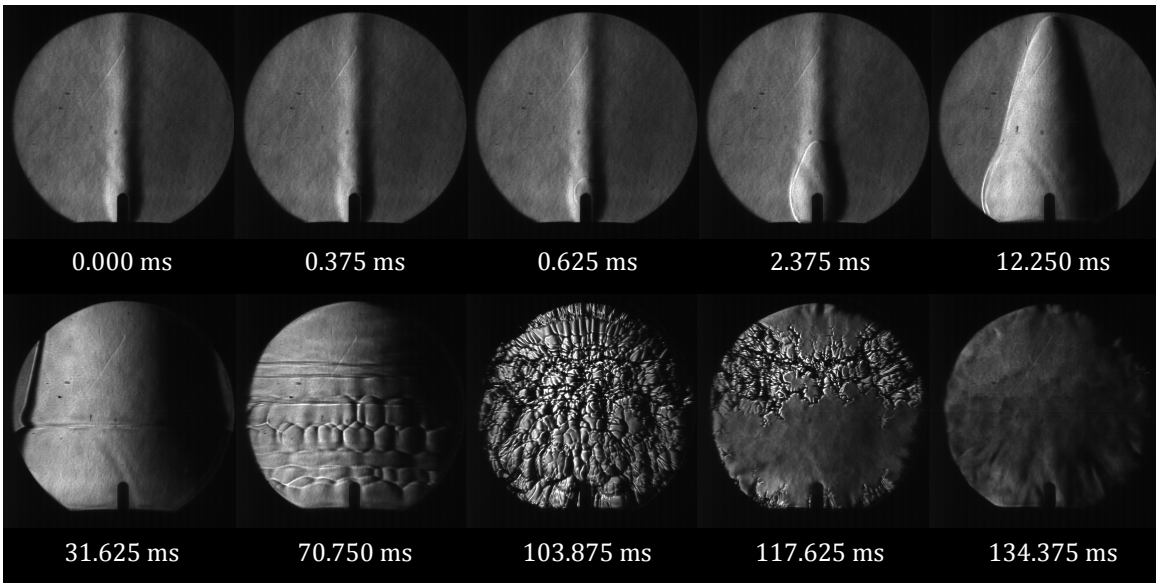

Figure 3.40: Schlieren visualization of a single flame ignited at the glow plug at 0.125 ms ($P_0 = 101$ kPa, $\phi = 1.74$)

3.5.5.1 Single Flames

Figure 3.40 shows schlieren images obtained using a vertical knife edge of a fuel-rich hexane air-mixture, $\phi = 1.74$, igniting at the top of the glow plug and propagating at different speeds in the horizontal and vertical direction. The high flame speed causes the flame to consume the entire vessel before any buoyancy effects change the shape of the flame. In most of the cases, ignition occurs at the top of the glow plug (see Appendix J for ignition locations from various experiments), with some experiments igniting on the side of the glow plug where the temperature is slightly higher than at the top (see Sections 3.2.3 and 3.2.4) and very lean mixtures igniting in the plume above the glow plug. Additionally, the region of reverse curvature (frame 5 of Figure 3.40) develops the initial instability leading to a highly wrinkled flame before the flame front reaches the windows. The growth of these instabilities is a function of the composition and curvature of the flame, which will be elaborated in

the next section. The initial region of curvature change is due to the flame propagating out of the plume produced before ignition, which would not be present in typical spark ignition experiments.

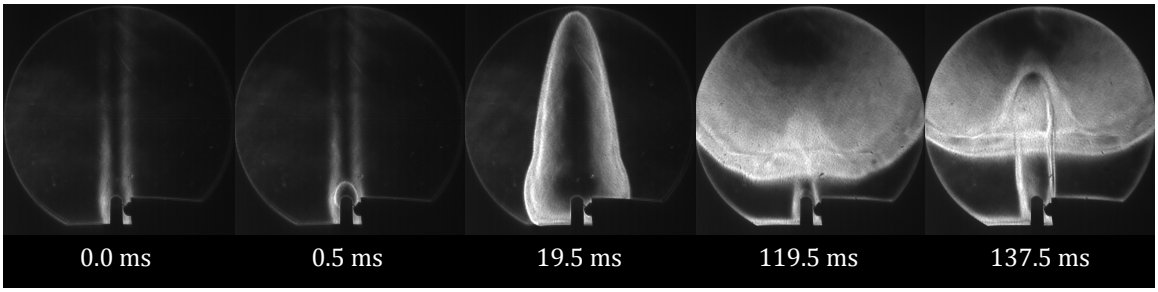

Figure 3.41: Schlieren visualization of a sequence of two flames ignited at the glow plug at $t < 0.5$ ms and 119.5 ms ($P_0 = 101$ kPa, $\phi = 2.25$)

3.5.5.2 Multiple Flames

As the equivalence ratio is increased for rich mixtures, the flame propagation speed is reduced and we observe that the flame is lifted away from the glow plug by buoyancy and the second flame ignites in its wake. Visualization of the flame is crucial to observe multiple ignitions and their timing. Figure 3.41 shows the established plume above the glow plug in a dark background schlieren image and the two successive ignitions at $t < 0.5$ ms and 119.5 ms. Depending on the flame speed, the re-ignition can occur again with the inflow from the second flame extinguishing the flame at the glow plug, or the flame transitions to a puffing flame. Multiple flames are a special case of the puffing flames and like those, a characteristic frequency can be assigned. When investigating the dependence of the frequency on various parameters, they are considered together with continuously puffing flames.

3.5.5.3 Puffing Flames

For even richer mixtures, continuously puffing flames are observed as shown in Figure 3.42. The flame ignited at the glow plug and propagates outward, slowly on the sides and quickly on the top due to the different temperature. The puffing flame is created by the interaction of the flame propagation and the flow field. Three different effects contribute the flow field outside the flame. The volumetric expansion across the flame front creates a dilatation flow that pushes the unburnt gas outside the flame outward. Second, the burnt gas has a lower density and buoyancy accelerates the flame upward creating an entrainment flow at the bottom of the flame. Finally, the density gradient across the flame front is misaligned with the hydrostatic pressure gradient, which leads to

the creation of vorticity from baroclinic torque. All of these effects combined create an inflow that exceeds the outward flame propagation leading to an instability of the flame front. The process, which is discussed in detail in the next chapter, repeats itself periodically until the temperature of the glow plug decreases sufficiently or the hot products, which fill the vessel from the top, reach the ignition source. The interface between burned and unburned gases is visible in the last four frames of Figure 3.42 and reaches the glow plug after 8 seconds.

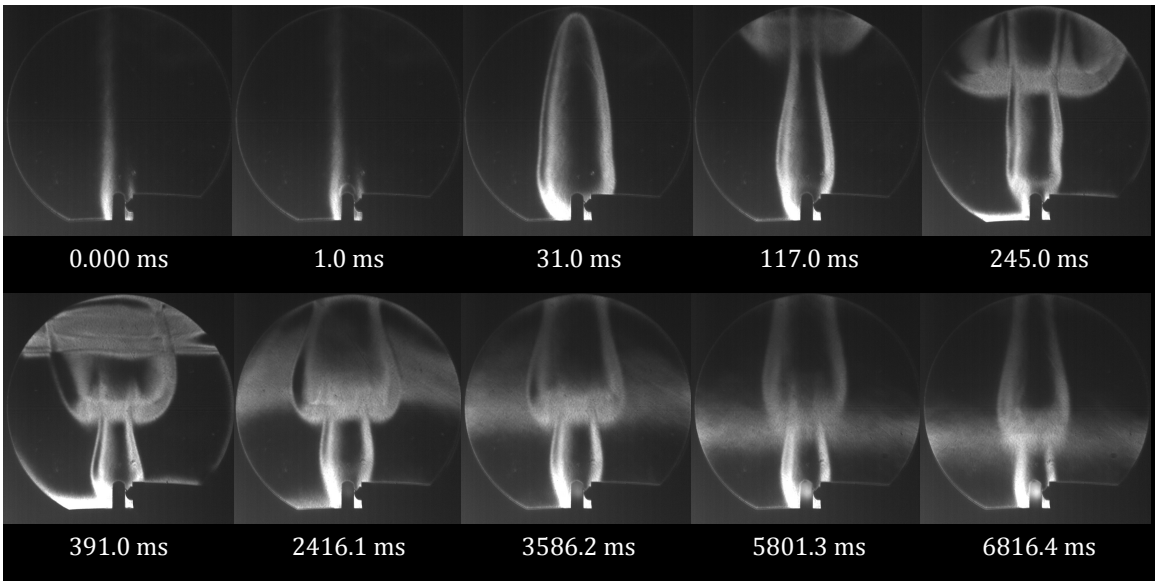

Figure 3.42: Schlieren visualization of puffing behavior (ignition at 1 ms, $P_0 = 101$ kPa, $\phi = 3.0$, shot 42)

3.5.5.4 Combustion Mode as a Function of Richardson Number

The different modes of combustion are a function of the flame propagation speed and the buoyancy of the burned gases. The buoyancy effect depends on the densities of the burned and unburned gas and the gravitational acceleration. We suggest that the different regimes can be characterized by the Richardson number, Ri, which represents the ratio of buoyancy to inertial effects in gas motion

$$Ri = \frac{AgL}{U^2} = \left(\frac{\rho_u - \rho_b}{\rho_u + \rho_b}\right)\frac{gL}{V_f^2} \tag{3.79}$$

$$Ri = \frac{\text{buoyancy}}{\text{inertia}} = \frac{\Delta\rho g L}{\bar{\rho} V_f^2} \tag{3.80}$$

where A is the Atwood number based on the unburned and burned gas densities (ρ_u and ρ_b, respectively), g is gravitational acceleration, L is the height of the glow plug, and U is the measured

horizontal flame propagation velocity (V_f). Figure 3.43 shows how the Richardson number changes with the mixture composition. We observe a single flame when the Richardson number is below 0.4 (see region II in Figure 3.43) with the exception of the 4 lowest equivalence ratios (region I).

In region I near the lean limit, we observe a different ignition and flame propagation phenomenon. As we approach the lean limit the ignition temperature is raised to above 1170 K, which increases the size of the plume and ignition is not observed in a small kernel, but in the plume. The flames propagate quickly in the hot plume and consume the entire volume. This phenomenon is observed in shots 28, 30, 36, and 37 with mixtures ranging from $\phi = 0.59$ to 0.69. Images showing the ignition location are available in Appendix J and schlieren sequences in Appendix K. By adding hydrogen and lowering the ignition temperature it is possible to obtain puffing behavior as discussed in Section 4.3.5.

For Richardson numbers between 0.4 and 2.5 re-ignition occurs (see region III) and for value above 3.5 puffing flames are observed (see region IV). This suggests that when the buoyancy and inertia are of the same magnitude the flame transitions to re-ignition and further decrease in the inertia leads to puffing flames.

Although the correlation of behavior with Richardson number is reasonable, other explanation are possible, that are explained in more detail in the next chapter.

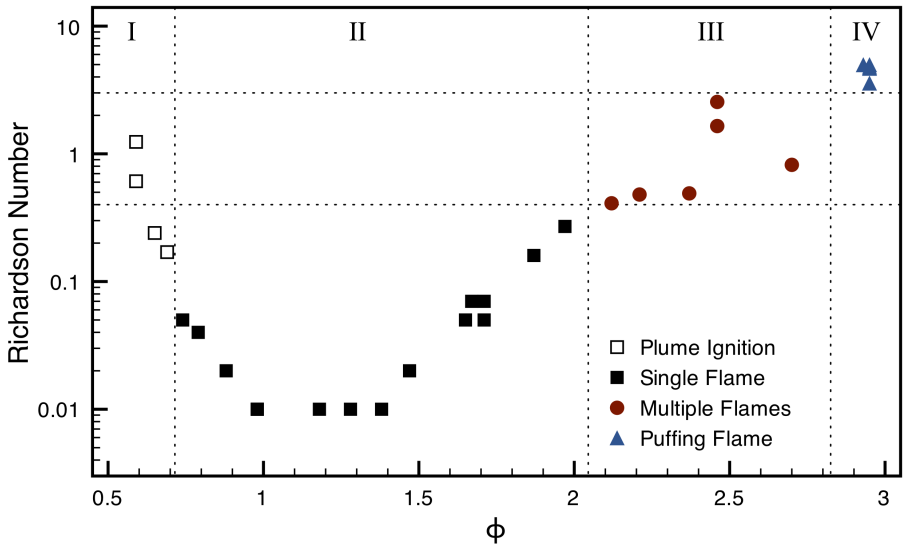

Figure 3.43: Ignition behavior as function of Richardson number for varying equivalence ratio at atmospheric pressure in the 2 liter combustion vessel

3.6 Conclusion

The ignition of gaseous n-hexane-air mixtures and subsequent flame propagation have been investigated by varying the mixture composition, initial pressure, and hot surface used to ignite the mixture. Consistent with the known lower flammability limit, the maximum temperature of the hot surface was insufficient at igniting the mixture. Away from the lower flammability limit, the ignition temperature is an almost constant value over a wide range of equivalence ratios ($0.75 < \phi < 2.7$) with large variations as the upper flammability limit is approached.

A simple model to investigate hot surface ignition is proposed based on the buoyancy driven flow along a vertical hot plate. In this situation, the fluid elements are entrained into the hot boundary layer, where the temperature increases as the elements move closer to the hot surface. Considering a large activation energy assumption, the dominant balance occurs between the diffusion and convection in the outer region of the boundary layer. In the inner layer, diffusion balances with the chemical reactions until ignition occurs. The effects of changing composition and initial pressure can be captured using this dominant balance approach. Further modeling of the ignition temperature has been done using tabulated detailed chemistry, which improved on capturing the lower flammability limit, but is still limited by the available low temperature reaction mechanisms, which are particularly sparse for n-hexane, and indicate an opportunity for future research. A limited study of the effect of hot surface area also indicates an area of future research. However, the limited experiments performed show that some historical data indicates ignition temperatures that are significantly higher that observed in the current study.

The flame propagation that follows the ignition has been studied can compared to simulations results and literature values. Over the range of equivalence ratios investigated three distinct modes of combustion are observed: single flame, multiple flames, and puffing. These regimes are captured by considering the competition between inertia, i.e., flame propagation, and buoyancy, which can be expressed in the Richardson number. The various regimes are clearly delineated by the Richardson number and give a direction for studying the puffing phenomenon in detail in the next chapter.

This page intentionally left blank.